

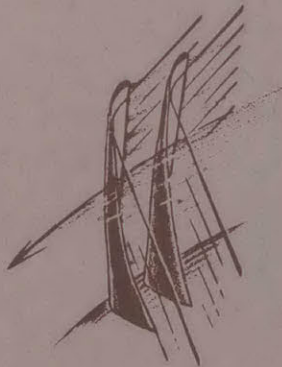
*For Xeroxing
copy*

STALLED FLOW PERFORMANCE OF A SINGLE
STAGE TRANSONIC COMPRESSOR

by

F. G. Bartlett, Jr.
E. M. Greitzer

GT&PDL Report No. 144 December 1978



GAS TURBINE & PLASMA DYNAMICS LABORATORY
MASSACHUSETTS INSTITUTE OF TECHNOLOGY
CAMBRIDGE, MASSACHUSETTS

STALLED FLOW PERFORMANCE OF A SINGLE
STAGE TRANSONIC COMPRESSOR

by

F. G. Bartlett, Jr.
E. M. Greitzer

GT&PDL Report No. 144 December 1978

This work, carried out in the Gas Turbine and Plasma Dynamics
Laboratory, was supported by the NASA Lewis Research Center under
Grant NGL 22-009-383.

ABSTRACT

The stalled flow performance of a single stage transonic compressor is examined, using data from the MIT Gas Turbine Laboratory's Blowdown Compressor Facility. Measurements of the blowdown corrected weightflow are included, as well as stage exit static to inlet total pressure rise, and rotating stall cell measurements. A comparison of the flow blockage, as represented by stall cell circumferential extent, with the blowdown corrected weightflow is made. The 100% design speed stalled flow performance characteristic is presented. Radial traverse data is also presented including flow angles, static and total pressures, and Mach number components.

TABLE OF CONTENTS

	<u>PAGE NO.</u>
INTRODUCTION	4
DATA REDUCTION METHODS	10-27
Analog Data	10
Digital Data	17
A/D Process	18
Data Reduction Programs	20
RESULTS	27-40
Performance Characteristic	27
Blowdown Performance	28
Circumferential Extent of Stall Cell	30
Stalled Flow Performance	32
Stall Cell "Splitting" Phenomenon	33
Radial Traverse Flow Data	36
CONCLUSIONS	40
APPENDIX A: Uncertainty in Hand-Calculated Weightflow	44
APPENDIX B: Results of Fourier Analysis Routines	47
REFERENCES	48
FIGURES	49-79

INTRODUCTION

The relationship between pressure rise and weightflow for reasonably well designed axial compressors operating at constant speed near the design point is generally smooth and continuous, with negative slope. Thus, as the compressor is throttled, the pressure rise increases, until the existing steady axisymmetric flow pattern deteriorates. At this point (and with further reduction in weightflow) two phenomena may appear: surge and/or rotating stall (see figure 1). Surge is characterized by large fluctuations in the annulus averaged throughflow throughout the entire compression system, while in rotating stall, one or several patches of extremely stalled flow propagate around the circumference with the annulus averaged throughflow remaining constant. Rotating stall may appear as either part span or full span stall as in figure 1.

The throughflow in these stalled patches, or stall cells, is severely reduced and can even be slightly negative, i.e., from back to front. These stall cells can be approximated as regions of (zero flow) flow blockage which effectively reduce the available annulus flow area in proportion to their size. In contrast, the throughflow in the unstalled part of the annulus is not drastically reduced--the flow rate can be greater than the design rate. Therefore, a reduction in the annulus averaged throughflow while the compressor is exhibiting rotating stall should manifest itself as an increase in the stalled fraction of the total annulus. In other words, changes in weightflow should be associated with consistent

changes in the extent of the stall cells; an increase in weight-flow should be manifested by a decrease in stall cell extent, and vice versa. One aspect of this work will be to investigate this concept (with stall cell circumferential extent at the tip representing stall cell extent and flow blockage) for a low hub-tip ratio single stage transonic compressor.

By far, the majority of published research in this area has been done on subsonic compressors, and there are several reasons for this. Operation in the stalled flow regime is characterized by such adverse effects as high stress levels and exceedingly low efficiencies, with possibly elevated temperatures. The appearance of stalled flow can also be accompanied by surging of the entire compression system -- large-scale fluctuations of the annulus averaged throughflow. The combined effects of extended operation at low efficiencies and high temperatures, with periodic disturbances and large scale fluctuations in weightflow, can often be catastrophic due to the high stress levels. In stages with high speed transonic rotors, typical of fans in turbofan engines, these effects compound an already critical stress problem. Thus, high speed rotor testing for extended periods under adverse conditions is a demanding task.

The MIT Gas Turbine Laboratory's Blowdown Compressor Facility offers a means of obtaining stalled (as well as unstalled)

flow data from full-size (approximately 0.3 meter tip radius) transonic compressor geometries without sustaining these large stresses for extended periods. The purpose of this present work is to document the stalled flow performance of a transonic stage which has been the subject of a number of other studies in the blowdown facility. The goal here is to obtain, from existing data for this stage, the stalled portion of the compressor design speed performance line. In addition, the characteristics which are unique to stalled flow will be presented.

Previous Work on MIT Blowdown Transonic Stage

The MIT Blowdown Compressor Facility has been in operation since 1972. The complete details of this facility can be found in Reference 1, while an outline of its features will be presented in a later section.

The 59 cm. diameter, free vortex, transonic "MIT Rotor" with a design tip Mach number of 1.2 and total-to-total pressure ratio of 1.6, was designed in 1972 by Kerrebrock, as presented in Reference 1. At this time, design parameters for a matching free-vortex stator were also presented. However, final design of the stator was made only after experimental measurements were made on the isolated rotor, and the experimental flow angles were used in the final stator design, completing the "MIT Stage."

Investigations of the isolated rotor are presented by Epstein, Reference 2; and Thompkins, Reference 3. In Epstein's work, quantitative flow visualizations of the inter-

blade passage density fields for the transonic rotor are presented. Some remarkable pictures of tip, passage, and lambda shock structures for the MIT rotor are included. In Thompkins' work, carried out at approximately the same time, a computational and experimental study of the rotor flow field is presented. Time resolved data on the blade passing time scale is presented, as well as radial variations in mean flow data. The results show that the flow follows the free-vortex design only in the inner half of the annulus, with the flow changing to forced vortex type towards the tip.

In 1976, Farokhi, Reference 4, used the results of Thompkins' work to design a matching stator, completing the MIT Stage. The first detailed measurements of the mean flow from the stage were presented by Figueiredo in Reference 5.

Overview of Work to be Presented

In this present work, the stalled flow performance of the MIT blowdown transonic compressor stage is examined. In the following sections, an outline of the MIT Blowdown Facility and its instrumentation, as applicable to this study, is presented. A description of the required data manipulations in both analog and digital form is included. Measurements of the blowdown weightflow history, and stage static-to-total pressure rise, as applicable to the determination of compressor performance, are presented, as well as some measurements of the flow which are characteristic of stalled runs, including rotating stall cell measurements.

THE FACILITY

Although the MIT Blowdown Compressor Facility has been fully described in Reference 1, a brief description is included here for background. This facility offers a means of testing full-size transonic rotors and stages at reasonable costs. As the name implies, the tests run are not continuous, but are rather short duration blowdown runs, in which all data is recorded during a time interval of the order of 100 milliseconds. The test set-up is outlined as follows (see figure 2): a large supply tank (4.3 m^3) is followed by a short annular test section (approximately 1 m. long by .3 m. diameter) which houses the transonic stage. The test section is followed by a large dump tank, whose volume is roughly 3 times that of the supply tank. Initially, the supply tank and test section are separated by a thin (0.5 mm) aluminum diaphragm. The sealed supply tank contains the test gas mixture at a pre-determined initial pressure, while the test section and dump tank are initially evacuated. An orifice plate, which will choke during the test, separates the test section from the dump tank. Upstream of the rotor in the test section, an annular bleed duct is located to remove the boundary layer flow, which is vented through separate choked orifices into the dump tank. These orifices are set to maintain the bleed flow at 10% of the test section flow.

The test gas used in runs from which the data used in this report was taken was an 18% freon/82% argon mixture, which yields a ratio of specific heats of 1.4, a gas constant

of 148.2 Joules/kg-°K, and thus a room temperature sonic velocity of approximately 72% that of air.

Before a test is run, the rotor is brought up to speed in essentially vacuum condition, and thus requires minimal power expenditure. When the test is run, the aluminum diaphragm is explosively opened, and the test gas is allowed to flow through the compression system. During the few hundred millisecond test, the rotor is not powered, but rather decelerates at a rate governed by the gas dynamic loads and the rotor inertia. Since the stage inlet total temperature is also dropping during the test, the rotor inertia and initial supply tank pressure can be tailored to result in a constant tip Mach number during part of the transient blowdown test. The choked exit orifice and the fixed geometry test section should, therefore, maintain a fixed axial Mach number for as long as the orifice is choked. In this manner, during part of a test with fixed tangential and axial Mach number, steady state aerodynamic data can theoretically be obtained from a basically transient blowdown process.

The instrumentation used to gather the data which is analyzed in this work is of two types: fixed position and traversing probe data. The fixed position pressure transducers are themselves of two types: low frequency response (0-1000 Hz) strain gage Statham-type pressure transducers, and high frequency response (0-100 kHz) exposed silicon diaphragm Kulite type pressure transducers. The low-frequency transducers

recorded the supply tank pressure, stage inlet wall static pressure, stage exit wall static pressure, and dump tank pressure. The high frequency response transducers recorded the wall static pressure just upstream of the rotor, and data from these transducers was used to make stall cell measurements.

The next section describes in detail the data reduction procedures that were used. The methods used to reduce the analog data are first presented. A discussion of the analog/digital procedure and subsequent processing of the digital data is then given, with observations of the results following the latter.

DATA REDUCTION METHODS -- ANALOG DATA

Oscillograph Charts

All of the data examined in this work was primarily stored as analog voltage signals on magnetic tape. Some of the data was converted to digital form before further data reduction. The remainder of the data was manipulated in analog form, and was read off of tape onto 17.8 cm. wide light sensitive oscillograph charts. The time scale of each chart can be set by choosing the appropriate tape recorder playback speed and chart speed and can be suited to the time scale of interest.

Single and Multi-Channel Data

The types of analog data examined are basically in two groups: single and multi-channel data. The single channel data represents continuous information from a single pressure transducer, and the multi-channel, or multi-plexed, data represents discontinuous periodic information from a number of pressure transducers (usually 4 to 6). Ideally, all of the data should be stored on its own channel, but over the time span that this data was recorded, the facility's data acquisition system was restricted by the 14-channel FM tape recorder. Thus, some of the data was multiplexed and stored as a single channel. This multiplexed signal can best be described as a periodically piecewise-continuous signal, with each continuous piece representing information from a single transducer. A plot of a digitized version of a segment of one of these signals is shown in figure 3. The time scale of the figure is greatly expanded from a typical oscillograph chart of the same signal, on which each channel appears as a point rather than as a step. Thus, a digitized version is presented to show the details of the signal. The figure shows approximately 2 multiplex periods, each period containing 6 channels of information. A multiplex period is typically 1 millisecond long. The channel at the +1.0 volt level is a constant reference voltage, and the following channels represent the supply tank pressure, stage inlet pressure, stage exit pressure, dump tank pressure, and traversing probe position, respectively. These are all of the types of information

recorded as multiplex signals which are examined in this work. The transducers are all linear, their sensitivities are all known accurately, and the initial values of all quantities measured are known. Thus, measuring the multiplexed data by hand from the charts, channel-by-channel, is done in a straight-forward manner.

Weightflow Calculation

Of primary interest in this data is the supply tank pressure, from which the blowdown weightflow is calculated. A description of this calculation is included in a later section. This calculation requires the evaluation of the rate of change of pressure in the supply tank. When done by hand (as opposed to machine operation on digitized data), this calculation is carried out by measuring the data on the charts at 10 millisecond intervals with divider and scale. The measured values are then used in a simple centered three-point finite difference approximation for the pressure derivative.

High Frequency Wall Static Pressure Data

Single channel data gives more detailed information. High frequency Kulite-type diaphragm wall static pressure transducers, mounted just upstream of the rotor, provide much information. In some runs, 3 of these transducers were mounted circumferentially at 0° , 77° , and 180° . The data from these transducers is used to make stall cell measurements, as well as for measuring rotor speed. Rotor speed can also be determined from a recorded tachometer signal, but it was found to be adequate to read it from the high frequency wall

static pressure transducers, since the tip shocks appear quite noticeably in the high frequency wall static data, as in figure 4. Thus, the speed of the 23 bladed rotor can be determined with the desired precision on an expanded time chart. (In contrast, the recorded tachometer signal has 460 pulses per revolution, or 20 per blade passing. Measurement of this signal requires a greatly expanded chart time scale, which is unnecessary if the high frequency wall static pressure data is available.)

Constant Tip Mach Number

Verification of constant corrected rotor speed, or tip Mach number based on inlet total temperature, during a test is made from the rotor speed and supply tank temperature. Since the flow between the supply tank and stage inlet is assumed isentropic, and unsteady effects can be shown to be small, this is also the inlet total temperature. This temperature is determined from the supply tank pressure using the isentropic relationship and the known initial temperature and pressure:

$$\frac{T_1}{T_1(0)} = \left[\frac{P_1}{P_1(0)} \right]^{\frac{\delta-1}{\delta}}$$

The tip Mach number is evaluated as follows:

$$M_T^2 = \frac{U_T^2}{a^2} = \frac{\omega^2 r_T^2}{\delta R T_1} = \frac{(\omega/\omega(0))^2}{T_1/T_1(0)} \cdot \frac{r_T^2 \omega(0)^2}{\delta R T_1(0)}$$

or

$$M_T^2 = M_T^2(0) \frac{(\omega/\omega(0))^2}{T_1/T_1(0)}$$

therefore, constant tip Mach number is assured as long as the ratio

$$\frac{(\omega/\omega(0))^2}{T_t/T_t(0)} \quad \text{is constant.}$$

For the 100% design speed runs, with

$$\delta = 1.4, \quad R = 148.8 \quad \text{Joule/Kg-}^\circ\text{K}, \quad T_t(0) = 294^\circ\text{K},$$

$$\omega(0) = 166 \cdot 2\pi \quad \text{SEC}^{-1}, \quad r_t = 0.295 \quad \text{METER}$$

the initial tip Mach number is 1.24.

Stall Cell Measurements

Stall cells can be detected very clearly with the high frequency wall static pressure transducers. The tip shocks do not appear inside of the stall cells, which are regions of greatly reduced throughflow, so that the stall cells appear as "shadows" over the tip shocks of the unstalled flow, as indicated in figure 4. This figure also illustrates the manner in which stall cell number, rotational speed, and circumferential extent at the tip were determined. First, the number of cells must be determined. From the known angular separation of the pressure transducers, and the measured phase separation of the stall cells passing successive transducers, the number of stall cells N can be determined (see figure 4):

$$2\pi \cdot \frac{\Delta T}{T} = N \cdot \Delta \theta$$

The stall cell absolute rotational speed then follows directly as,

$$\omega_s = \frac{1 \text{ REV}}{N \cdot T} \cdot 2\pi$$

and the extent of the stall cell is $DT\omega_s$ where DT is defined in Figure 4.

5-Hole Traversing Probe Data

Another type of analog data examined in this work is from a 5-hole spherical traversing probe. The radial traverse flow data is from a 5-hole spherical probe with cavity mounted silicon diaphragm pressure transducers. The details of this probe, and its calibration, is the subject of Reference 6. The calibration tables, as presented in this reference, were used to reduce the probe data into free-stream flow angles, static and total pressure, and Mach number components as averaged over several blade passing periods. This part of the data reduction was straightforward. However, converting the probe diaphragm voltage signals into pressures was not as direct, as the probe mounted pressure transducers were subject to thermal-based zero voltage drift. Thus, reduction of the probe diaphragm voltage signals required the use of a drift correction scheme. Two correction schemes are described in detail in Reference 5. The one which was used in this work, along with a slight modification, will be briefly described here.

The zero voltage drift is assumed to be a function of the probe heat transfer characteristics, an analysis of which is detailed in Reference 5. It is argued that the correction for this thermal based drift is proportional to the

current exciting the 5 diaphragms, with the constant of proportionality unique to each diaphragm. Thus, the voltage output from each diaphragm is assumed to be the sum of two inputs: $V_i = \alpha_i P_i + \beta_i f(I)$ where V_i is the voltage output of diaphragm i , P_i is the pressure at diaphragm i (the probe body is referenced to vacuum), $f(I)$ is a voltage signal proportional to the total probe excitation current, and α_i and β_i are constants of proportionality which must be determined. This equation can be rewritten, solving for the pressure,

$$P_i = \frac{V_i - \beta_i f(I)}{\alpha_i}$$

or

$$P_i = \alpha'_i V_i + \beta'_i f(I)$$

$f(I)$ and each V_i are recorded during the test, and the constants α'_i and β'_i can be determined from two boundary conditions at which the value of pressure is known. For the blowdown test, these boundary points are: (1) the moment before the probe body leaves the wall, at which time all 5 diaphragms are assumed to be measuring the wall static pressure; and (2) at a time near the end of the blowdown when the throughflow has stopped, at which time the pressure is also known from the Statham instrumentation. In this manner, pressures from all 5 diaphragms can be retrieved during the traverse.

A further modification of this method was required in some of the runs, namely those in which the current signal, $f(I)$, had not been recorded. It was noticed that the probe diaphragm signals for different runs were similar, except for a difference in time scale. Thus, it was possible, by determining the time scale factor (by comparing the diaphragm signals from two runs) to use the probe current signal from another run, allowing the correction scheme to be applied.

DATA REDUCTION METHODS -- DIGITAL DATA

A primary consideration in choosing to digitize the data was the uncertainty in the hand-reduced weightflow calculations introduced by the resolution of the measured data. The difficulty lies basically in the evaluation of the local slope of the experimental data. A simple error analysis of the procedure used (presented in Appendix A) shows that even if the supply tank pressure can be determined with 1% accuracy, the mass flow could be in error by as much as 20%. Achieving accuracy better than 1% with the strip charts does not appear likely; at least not an order of magnitude better. A better alternative is to employ a more extensive curve fitting scheme in the neighborhood of each point. Using a computer in such a scheme, one can employ the curve fitting procedures necessary to determine the slope of the data, and many runs can be examined in a reasonable amount of time once the data reduction programs have been written. This capability is highly desirable, since obtain-

ing the stalled flow portion of the design speed line for this stage requires the reduction of a number of blowdown runs. Machine manipulation also permits the comparative use of alternative reduction methods, which helps determine the effect of any given reduction scheme on the end results.

The A/D Process: Preparation and Testing

An outline of the A/D Process is shown in the top of figure 5. The data was played back on the facility's Ampex Model FR-1900 14-channel wide band FM tape recorder, with frequency response DC to 80 kHz at 120 ips, and 40 dB signal to noise ratio. The tape heads were checked and cleaned before the A/D sessions, a step which was important in achieving useable data. The data was played back at half speed, 60 ips, and the signal was passed through a 10k low pass filter before transmission to the A/D converter. A multi-speed A/D test was made to determine the optimum playback speed. The results were simple to evaluate; the facility's low-speed A/D system works well at playback speeds of 30 ips and 60 ips, and not at all at 120 ips. The quality of the signal converted at the lower speeds is identically high, and 60 ips was chosen for the A/D conversion.

A second test was made to determine the effect of the low pass filter on the multiplex signal (the multiplex

signal is described in a previous section). This test was carried out at the same three speeds as above. Direct observations of the multiplex signal on a standard lab oscilloscope determined that signal identity is lost at 60 ips with 5k low pass filtering, but is maintained with 10K low pass filtering at the same speed. (By modeling the multiplex signal as a square wave and carrying out a Fourier analysis, similar results were obtained.) The results of the test for the 60 ips playback speed with 10K low pass filtering is presented in figure 6 and can be compared with figure 3 which shows the same data with no filtering. As is evident in these figures, the signal voltage level is unaffected by filtering. Signal definition is quite adequate in the filtered data, although the sharp leading and trailing edges of the signal is lost. The remaining signal definition is, however, quite adequate for the demultiplexing routine which is described in a later section.

A/D Converter

The effective sampling rate of the GTL low speed single channel A/D converter is 100,000 Hz, or one point every 1/100th millisecond of test time. The sampling rate is determined by a trigger pulse, whose frequency is modulated by the tape recorder playback speed. The A/D converter has ten-bit resolution, or .1% full scale (1 part in 1024). Full scale is +/- 2.5 volts, so the converted signal has a resolution of .005 volts. The A/D interface program which was used, however, sacrifices the least significant 2 bits of

resolution, so that two 8-bit data points can be packed into one 2-byte word, making the most efficient use of high speed memory, and allowing more data to be recorded from each test. Even so, only the first 160 milliseconds of each test could be recorded this way, with data taken every .01 millisecond. Data taken every .02 milliseconds would not adequately define the multiplex signals. The effective resolution of the digitized data is .4% (4 in 1024), or .020 volts.

The existing GTL A/D interface programs were utilized to create a data set of digitized multiplex signals upon which all further data manipulation was carried out.

The Data Reduction Programs

An outline of the relationship of the data reduction programs is presented in figure 7. The remaining data manipulation would have been much more direct had the desired data not been recorded as multiplexed signals. However, in order to take advantage of the large amount of existing data for this stage (which was recorded in this manner to allow maximum utilization of the 14-channel FM tape recorder), it was decided to deal with the multiplex signals, and so, a de-multiplexing routine was created.

De-Multiplexing Routine: MPLEX

The structure of the multiplex signal has been illustrated in a previous section. Since not all of the runs had the same number of channels, nor did they appear in the same order, the de-multiplexing routine was made to allow

flexibility in defining the data channels. All of the multiplex periods were roughly one millisecond long, so that the data points for each of the measured channels could be measured approximately every millisecond.

The trailing edge of the reference voltage serves to define the beginning of each multiplex period. This point is found for each successive period in two steps. First, a 5-point interval (.05 millisecond) that has an average voltage which falls within some narrowly defined neighborhood of the reference value, and whose standard deviation of the sample does not exceed some small value (3% full scale worked well for this data) is found. Next, succeeding points are tested to determine the point at which the data deviates from the reference voltage by some specified value. This defines the trailing edge of the reference channel as the period boundary. Checking the standard deviation of the sample helps to insure that the 5-point interval does not merely randomly average out near the reference voltage value. This scheme has the advantage that should the routine not be able to find the next multiplex period because of noise, that period is skipped, and the next "clean" period is found.

Each of the data windows following the period boundary is characterized by two time intervals: (1) separation from the period boundary; and (2) its width. These intervals are defined by examining a typical period (as shown in figure 8). A typical width for each window is .08 to .1

milliseconds, or 8 to 10 data points. The routine allows for two methods of evaluating these 10 points. The first is strictly to average them. The second is to average, find the standard deviation of the sample, and throw out points which deviate by more than, for example, 2 standard deviations from the sample. This second method is an effective means of filtering the data from isolated random noise, and is more suitable if the data window as defined misses the actual window by one or two points.

The value determined by either of these methods is assigned to a time corresponding to the midpoint of the interval. In this manner, all or part of each run's 160 milliseconds of multiplex data is broken up into discrete channels of information, upon which further data reduction can proceed.

120 Hertz Noise (60 Hertz Playback Time Scale)

The results of the demultiplexing program were then Fourier analyzed and reconstructed with interfering signal frequencies filtered out. This was necessary since there was an approximately 120 Hz uniform amplitude signal superimposed on all of the data. This signal bore no relation to the fluid mechanics of the situation since:

- (1) The signal had constant amplitude and frequency during the test, although the supply tank pressure drops to roughly half of its original value. If the signal were associated with unsteady wave phenomena in the supply tank, the amplitude would be expected to scale with the density, and hence decrease with time.

(2) The same signal appears on the channel representing the traversing probe position, which is known to be constant between 0 and 50 milliseconds and beyond 120 milliseconds. The phase of these 120 Hz signals match up exactly on the supply tank pressure and probe position channels, showing that the source is electrical in nature.

Fourier Analysis Routine (FORAN)

A Fourier analysis routine was created to break the data down into component frequencies, reconstruct the data without the interfering signal frequency, and replace the original data with the unfiltered data. This routine was broken into 3 program units, FORAN1, FORAN2, and FORAN3, so that the intermediate results could be evaluated before replacing the results of MPLEX with filtered data.

In FORAN1, the data segment, typically 150 milliseconds long and consisting of 150 points, is divided evenly into 200 intervals, and the data is linearly interpolated at each of the resulting 201 points. Then, a straightforward Simpson's Rule integration scheme is applied to evaluate the required Fourier series coefficients, having defined the data curve as an even function. (Application of Simpson's Rule requires that the data lie on exact intervals, which is why the actual data points were not used. An integration scheme other than Simpson's Rule could also have been used, but the chosen method was exceedingly simple and gave excellent results, so no other method was tried.) This program plotted the frequency/amplitude spectrum of the data, and also plotted

the reconstructed data curve, verifying that an accurate representation of the data had occurred.

FORAN2 reconstructs the data set from the coefficients found by FORAN1, and selectively sets the coefficients to 0 of those frequencies which are to be filtered out. The filtered reconstructed data set is plotted. See Appendix B for examples of the results of these routines.

Finally, if the results of the Fourier analysis are adequate, the results of MPLEX are replaced with the filtered reconstructed results of FORAN2 by running FORAN3.

Weightflow Calculation

The results of MPLEX, either filtered or unfiltered, can next be used to calculate the actual and corrected weightflow. There are at least three methods of evaluating the weightflow, as described in Reference 1. The first is based on the rate of change of pressure in the supply tank. The second assumes uniform isentropic flow to the stage inlet face, and uses the inlet wall static pressure, supply tank pressure, and the known flow area, to evaluate the weightflow. In the third method, the stage exit flow area and the downstream choked orifice area are used to obtain the weightflow.

Note that all of the methods depend on one dimensional (uniform) isentropic flow assumptions. However, the flow can only be considered isentropic and uniform upstream of the stall cell potential field. The second and third methods, therefore, cannot be used for runs in which stall cells appear. The first method is thus the most reliable of the three for these conditions.

The weightflow leaving the supply tank differs from the weightflow through the test section by the amount of boundary layer bleed flow. A separate choked orifice maintains this at approximately 10% of the test section flow. However, the exactness of this figure, and its constancy during the tests, are both not critical, since an error of 10% would only affect the weightflow calculation by 1%.

The weightflow leaving the supply tank is evaluated, using continuity, from the rate of change of density (ρ) in the supply tank:

$$W = \frac{d}{dt} \int \rho_i dV_i$$

Assuming that the density is constant in the supply tank,

$$W = V_i \frac{d}{dt} (\rho_i)$$

Assuming the perfect gas relationship, $\rho_i = P_i / RT_i$, and also assuming that changes in the supply tank are isentropic so that,

$$\left[\frac{T_i(0)}{T_i} \right] = \left[\frac{P_i(0)}{P_i} \right]^{\frac{\delta-1}{\delta}}$$

one is finally led to

$$W = \frac{V_i}{\delta RT_i(0)} \left[\frac{P_i(0)}{P_i} \right]^{\frac{\delta-1}{\delta}} \cdot \frac{dP_i}{dt}$$

Since the test section flow differs from the flow leaving the supply tank by the fraction of boundary layer bleed, if we recognize the speed of sound squared term in the

denominator, one finally achieves,

$$W = \frac{V_1}{(1+\delta)a_1(0)^2} \cdot \left[\frac{P_1(0)}{P_1} \right]^{\frac{\delta}{\delta-1}} \cdot \frac{dP_1}{dt}$$

where W is the weightflow, V_1 is the supply tank volume, δ is the fraction of boundary layer bleed flow, $a_1(0)^2$ is the initial speed of sound in the supply tank, $P_1(0)$ is the initial supply tank pressure, P_1 and $\frac{dP_1}{dt}$ are the instantaneous values of pressure and rate of change of pressure, respectively.

As is discussed in Appendix A, the pressure derivative, when evaluated by hand using a simple three-point centered finite difference approximation, has an unacceptable uncertainty. Using the digitized data, a better derivative determination can be made. Two methods of evaluation are available in the program MASFLO. The first performs a least squares linear fit in the neighborhood of each point (about 30 points) and the second performs a least squares parabolic fit. The results from either method are indistinguishable.

The weightflow is corrected to standard conditions, using the results of the curve fit at each point. The results of the weightflow calculation, along with the demultiplexed supply tank pressure and stage exit wall static pressure, are used to generate the stage performance data for each run. Since the supply tank is essentially an inlet plenum chamber, and the flow can, to a good approximation, be assumed isentropic between the supply tank and stage inlet, the supply tank pressure is also the stage inlet total pressure. The

stage exit wall static pressure is used to define the stage static delivery pressure. Note that for the runs exhibiting rotating stall, the exit pressure varies circumferentially with respect to the stall cell(s). The procedure used was to average both the corrected weightflow and exit static pressure over a time corresponding to a complete stall cell rotational period, to define a performance point.

All of the performance points obtained in this manner are used to define the stage performance map.

RESULTS

Performance Characteristic

The stage exit static to inlet total pressure ratio as a function of corrected weightflow is given in figure 9. The weightflow here is corrected to Standard Conditions of 1 atmosphere and 288.9°K. All of the data presented here are for 100% design speed operation. Figueiredo's data for Run 217 (reference 5) is also shown. Figueiredo's performance point was obtained from radial traverse data which was integrally mass averaged, as described in his work, and agrees well with the results found in this work. Figueiredo's investigation of the mean flow for this stage showed that the stator inlet setting angle is too shallow by as much as 10° so that the stator incidence angle is much too large over all flow conditions. Figueiredo's measured rotor adiabatic efficiency of 87% and stage adiabatic efficiency of 56% (for runs not exhibiting rotating stall) confirms that the stator

losses are excessively high. The observed performance characteristic, figure 9, indicates that this stage's performance is not typical of well-designed compressors since nowhere is there indicated a negatively sloped portion of the characteristic. Thus, the rotating stall data presented in this work may not be completely representative of, in all respects, more typical transonic stages.

Blowdown Performance

Plots of static to total pressure rise and corrected weightflow during the blowdown process are presented in figures 10-15. Figures 10 and 11 represent an unstalled run (Number 210); figures 12 and 13 represent Run 218, with 1 stall cell appearing; and figures 14 and 15 are for Run 216, with two stall cells appearing. The characteristic presented in figure 9 was obtained from data such as this for the indicated runs.

Comparisons of the blowdown corrected weightflow indicate that the unstalled run, Number 210, having the choked exit orifice with the largest flow area, exhibited the highest level weightflow; Run 216 (with the smallest orifice) exhibited the lowest weightflow; and Run 218, with an intermediate exit orifice, exhibited an intermediate weightflow level (when all runs are compared at the same test times, of course). This is consistent with the observation of two stall cells in Run 216, one stall cell in Run 218, and no stall cells in Run 210, since the stall cells are assumed to be related to flow blockage.

There appears to be another qualitative difference in the weightflow curves for these three runs. All three exhibit

an initial peak in weightflow at around 20 milliseconds, starting from zero weightflow at 0 milliseconds. However, the manner in which the compression system adjusts to the initial transient appears somewhat different in the three runs. (Note: Run 216 and Run 218 are plotted with the same vertical scale, while Run 210 is plotted with twice this scale.) Notice that in Run 216, there is a very noticeable oscillation in corrected weightflow with considerable magnitude. In Run 218, the oscillation is still noticeable, occurring at approximately the same times as in Run 216, but with a smaller magnitude. In Run 210, even accounting for the change in scale, the oscillations do not appear with either the same timing or the same magnitude.

These oscillations in corrected weightflow appear to be genuine characteristics of the compression system, and are not believed to be manifestations of the data reduction scheme used. These oscillations appeared independently of the type of curve fit to the supply tank pressure, from which the pressure derivative (and hence, weightflow) was evaluated. Least squares linear fits, and least squares parabolic fits were tried, with varying time intervals between 15 and 40 milliseconds. In addition, the oscillations are of much longer duration than would be caused by acoustic waves in the supply tank.

The period of these oscillations appear to be of the order of 50 milliseconds. A basic Helmholtz resonator type analysis of the compression system yields an expected period of the order of 100 milliseconds, while simple acoustic wave travel within the supply tank would indicate a

period of at most 20 milliseconds. Clearly, these analyses yield only order of magnitude agreement and some further analysis is needed to provide a better understanding of how these observed oscillations in weightflow relate to the blowdown method of compressor testing.

A comparison of the exit static to inlet total pressure ratio plots for the three runs shows very plainly the appearance of the stall cells in Run 216 and Run 218. In Run 218, a single part span stall cell appears, rotating at approximately 57% rotor speed, and in Run 216, two part span stall cells appear, moving at approximately 54% rotor speed. Thus, since the stall cell rotational speeds for these two runs are essentially equal, twice as many stall cells appear during the same interval in Run 216 as in Run 218, and are thus less well defined. Determination that the cells are part span, rather than full span, was made by examining the stall cell signatures of one of the five high response traversing probe pressure transducer signals. The strength of the stall cell signatures were noted to drop appreciably before the traversing probe had completed the traverse, while the stall cell signatures evidenced at the tip in the high frequency wall static data during the same time were unchanged.

Circumferential Extent of Stall Cell

An important concept in the analysis of rotating stall fluid mechanics is the idea of stall cell blockage -- the fraction of the annulus area which the stall cell occupies. To illustrate these ideas, figure 16 compares the corrected weight-

flow for Run 216 with the circumferential extent of the stall cell in degrees (at the tip) as measured from the stall cell signatures over the tip shocks in the high frequency wall static data. Figure 17 shows the same for Run 218. The weightflows for these runs are also shown. The purpose here is to show the relationship between flow blockage, as represented by the extent of the stall cells, and corrected weightflow. In general, a clear correspondence between low weightflow and large blockage, and high weightflow and small blockage, is seen to exist. It is important to notice, however, that a definite time delay is observed (approximately 1 rotor revolution) with changes in the circumferential extent of the part span stall cell consistently lagging behind the changes in corrected weightflow. Thus, there appears to be a finite time required for the part span stall cells to alter in response to changes in corrected weightflow, in this case approximately equal to 1 rotor revolution in duration. Similar transient stall cell response is reported in reference 8, although for a three stage subsonic, high hub-tip ratio machine. Apparently, rotating stall cells do not respond completely quasi-steadily to changes in weightflow, but exhibit a time lag which, for the observed part span stall cells, is of the order of a rotor revolution.

It should be noted that circumferential extent as measured at the casing is not an exact method of determining blockage, especially for part span stall. However, the only assumption that is made here is that the blockage, and hence weightflow, is in some way proportional to circumferential

extent. It would be desirable to have data on radial extent so that a more precise mapping of stall cell extent could be obtained, although this was not possible with the existing data.

Determination of stall cell circumferential extent for test times much beyond 200 milliseconds into each test (in the very low flow regime) with reasonable accuracy, is very difficult. The distinct quality of the stall cell signatures over the tip shocks in the unstalled flow deteriorates considerably so that precise determination of the edges of the stall cells cannot be made. However, examination of the data from the traversing probe, which at these later times has completed the traverse and is positioned next to the hub, indicates that only part span stall is evidenced; at no time is transition to full span stall indicated.

Stalled Flow Performance

The scales of figures 11, 13, and 15 do not allow detailed comparisons to be made between the stalled runs. To do this, the performance data was plotted using the parameter,

$$\frac{P_{\text{EXIT STATIC}} - P_{\text{INLET TOTAL}}}{\rho_{\text{INLET}} \bar{U}_{\text{ROTOR}}^2}$$

where ρ_{INLET} is the stage inlet density, and \bar{U}_{ROTOR} is the mean rotor speed. This is the same quantity used in reference 7 to correlate compressor performance in rotating stall. This plot is presented as figure 18, for Run 216 and Run 218. Each of the points plotted represents an average value over 1 or 2 stall cell passings. For both runs, the drop in performance

indicated corresponds in general to decreasing corrected weightflow during the test. This appears to be consistent with operation on a positively sloped performance characteristic.

Also indicated in this figure are two dashed lines at 0.11 and 0.17. These values are from the correlation for compressor performance in rotating stall, presented in reference 7. The lower line represents the predicted pressure rise at shut-off (zero weightflow) for full span stall, and the upper line represents the maximum pressure rise measured during part span stall in the experiments of reference 7. It can be seen that the measured values for the part span stall cells seen in these two runs fall reasonably well in or near the neighborhood defined by the correlation. It should be noted that the correlation did not include data from either low hub-tip ratio and/or transonic compressors. It appears, then, that the part span stalled flow performance of this low hub-tip ratio transonic stage, at least in terms of pressure rise, is somewhat lower than that of purely subsonic high hub-tip ratio stages.

Stall Cell "Splitting" Phenomenon

An observation of transition from a single cell to two rotating stall cells was made at the end of Run 218, at approximately 180 milliseconds into the test.

From the high frequency wall static pressure data ahead of the rotor, it is possible to observe both tip shocks on the blade passing time scale, and stall cell "shadows" over

these tip shocks (see figure 3). By examining the data from two adjacent transducers, such as P_8 and P_7 , it is possible to identify a given stall cell passing first one transducer, and then the next.

At the end of Run 218, immediately prior to the appearance of the second stall cell, a marked decrease in the strength of the tip shocks in the middle of the unstalled flow was observed. By the time this region had reached the next pressure transducer (77° away), it had grown to appear as a second stall cell in the middle of previously unstalled flow. Thus, it appears that the time required for a second stall cell to reach its full circumferential extent from an unstalled condition is, again, of the order of one rotor revolution. Also, it is important to realize that succeeding stall cells can grow in previously unstalled flow rather than by simply splitting. Thus, the term splitting is somewhat misleading when used to describe the phenomenon of multiple stall cell creation.

Run 216

Run 216 exhibited two part span stall cells and will be examined here in greater detail. The blowdown weightflow (figure 12) and stage exit static to inlet total pressure rise (figure 13) for this run has already been examined. Figure 19 is a composite plot of the low frequency pressure transducer data for Run 216, showing the relationships between the supply tank, stage inlet and stage exit wall static, and dump tank pressures. Note that as a stall cell passes, the stage inlet wall static pressure rises (indicating a drop in flow velocity)

and the exit wall static pressure falls, with the inlet total pressure roughly between.

A curve of 1.89 times the dump tank pressure is also included to indicate the useful test time. Where this curve crosses the supply tank pressure, the boundary layer bleed orifices can no longer be assumed choked, and hence, the bleed flow is no longer a constant 10% of the main flow. Thus, the test section weightflow is less precisely determined after this point. This happens at approximately 150 milliseconds into the test. The traverse time is also indicated on the figure. Referring back to figure 12, it can be seen that during this time, the corrected weightflow changes considerably. It would be desirable to have the traverse occur during a period in which the corrected weightflow was constant, so that radial distribution effects would be isolated from changes in weightflow. For example, the time slot between 100 and 150 milliseconds might be more suitable. However, stall data with the traverse occurring in this time slot was not available.

Tip Mach Number

Figure 20 is a plot of the change in inlet total temperature (as calculated from the change in inlet total pressure with the steady one-dimensional flow relationship) and of the change in rotor speed for Run 216. As can be seen, their ratio is constant during the traverse, and the indicated tip Mach number is,

$$(.90)^5 \cdot M_T(0) = (.90)^5 \cdot (1.24) = 1.18$$

which is within 2% of the design tip Mach number of 1.20.

Run 216 Radial Traverse Flow Data

Radial traverse flow data from a 5-hole spherical probe was examined for Run 216, which exhibited two stall cells, and hence the most stall cell passings during the traverse. Note that the traverse flow data is in the absolute reference frame, and the data was taken behind the rotor.

Flow Angles

Reference 9 presents detailed stall cell flow measurements from a low speed high hub-tip ratio machine, which could be varied from 1 to 4 stages (although the emphasis is clearly on multistage builds). It is emphasized that the performance of multistage machines can differ drastically from single stage machines. Some comparisons with the results from this work's single stage transonic low hub-tip ratio machine will be made.

Figure 21 is a plot of the (absolute) rotor exit tangential flow angles, Θ , for Run 216. On this plot, 0° is purely axial, and 90° is purely tangential. Test time, as well as radial location, is presented in all of the traverse flow data. The four dashed rectangles show the position of the stall cell at the tip as inferred from the high frequency wall static data.

The probe for this run was preset at a zero incidence angle of 45° . Where the plots are broken, the flow angles exceeded the useable range for the 5-hole probe. Four stall cell passings are seen here, although precise definition of the stall cell boundary is difficult to determine from the tangential flow angle data. Again, it must be remembered that here, radial

distribution effects, changing weightflow effects, and effects of the rotating stall cell are superimposed. However, the following result appears to be a manifestation of the rotating blockage only: as the stall cell is approaching the probe, the flow becomes increasingly more axial, while at the trailing edge of the stall cell, the flow has a very large, but decreasing, tangential component. This pattern is clearly repeated. Within the stall cell, the axial flow components are quite small (the flow is stalled). Thus, in the absolute frame, a large tangential component is evidenced. In reference 9, more detailed measurements using phase-locked ensemble averaging techniques show that the flow direction between the stalled and unstalled flow may differ by as much as 300° . For the cases investigated, it is reported that the unstalled flow behaved essentially as if no stall cell were present, while in the present work, there do appear to be changes in the unstalled flow.

The observation of higher axial flows on one side of the stall cell than the other is consistent with the mechanism of stall cell propagation. Consider the flow in the rotor relative frame. The stalled blade passages represent blockage to the flow approaching the blade row. Thus, flow is diverted to either side of the stall cell. The effect of this flow diversion is to increase the incidence of the flow on the blades "above" the (in the sense of suction side of one blade to pressure side of the next) stall cell, and decrease the incidence of the flow on the blades "below." Therefore, the blades above stall, and the blades below unstall, and the stall cell propagates

relative to the rotor. Each rotating stall cell thus has a stalling edge and an unstalling edge. In the absolute reference frame, since the stall cell propagation speed is approximately half of the rotor speed, the leading edge of the stall cell which the probe sees first is the unstalling edge, and the trailing edge of the stall cell is the stalling edge. Thus, in figure 21, the flow is seen to have a higher axial component on the leading edge of the stall cell (the unstalling edge).

Figure 22 is a similar plot for the radial flow angles. In this plot, positive angles are directed towards the tip, while negative angles are directed towards the hub. As can be seen the gross trend is, starting from near zero at the tip, increasingly positive flow angles towards the hub. This is consistent with the rotor geometry, which shows considerable annulus convergence. On the stall cell passing scale, the pattern is, as a stall cell approaches the probe, decreasingly positive flow angles, while in (or immediately after) the stall cell, large positive flow angles are evidenced. Again, this pattern is repeated, except near the tip where large radial fluctuations are probably inhibited by the wall. Large radial flows within the stall cell are also reported in reference 9.

Pressure Distribution

Figure 23 is a plot of the static pressure retrieved for Run 216. Here, the static pressure in and near the stall cell is seen to drop appreciably from the unstalled flow value. During the traverse, the inlet total pressure drops smoothly from about .40 to .35 atmospheres, so that the unstalled flow

has a static-to-total pressure ratio during the traverse which increases from approximately 1.1 to 1.3. The stalled part of the flow, however, has a much smaller pressure ratio. Figure 24 is a plot of the total pressure distribution behind the rotor for Run 216. The total pressure is seen to drop in the stall cells, while in the unstalled portions of the flow, the total-to-total pressure ratio varies between 1.5 and 1.6, except at the tip where the pressure rise is much less. This is similar with the results for low speed, high hub-tip ratio machines found in reference 9, in which a drop in total pressure is also consistently found behind the rotor in a stall cell.

Mach Number Distribution

Figure 25 is a plot of the total Mach number distribution retrieved for Run 216. It can be seen here that in the absolute frame behind the rotor, the Mach numbers near the stall cells in the unstalled flow are relatively high. Reference 9 includes part span stall measurements for a 2-stage machine which shows the unstalled flow direction becoming more axial as a stall cell approaches, but with the velocity remaining unchanged. Figures 26 and 27 are plots of the axial and tangential components of the total Mach number. Here, it is seen that the high Mach numbers in the stall cells are a result of the stalled flow having a large tangential velocity component. In figure 26, it is seen that, as a stall cell approaches the probe, the axial Mach number in the unstalled flow increases to a relatively high value, while as it passes, the axial Mach number is again increasing, but from the low value within the stalled flow.

The leading edge of the stall cell in the absolute frame was shown to be the unstalling edge, and the trailing edge the stalling side. This is consistent with the observed axial Mach number distribution. The tangential component, on the other hand, is relatively low until the stall cell appears. The stalled flow in the rotor relative frame then appears as a high tangential component in the absolute frame.

The gross trend of the unstalled behavior appears to indicate a relatively high tangential component at the tip, which then first decreases radially inward, and then again increases toward the hub. This trend is consistent with a combination of free-vortex flow distribution toward the tip of this machine as reported in the conclusions of reference 10 and shown in reference 9.

CONCLUSIONS

General

Perhaps the most important general conclusion is that the MIT Blowdown Compressor Facility is indeed a viable source of rotating stall data for high speed transonic compressors. In addition, when examining data from this facility, the nature of the blowdown process must be carefully accounted for in evaluating the results. When planning radial traverse data acquisition, it is imperative that the traverse be carefully timed to occur during an interval in which the corrected weightflow is truly

steady, while completed before the flow regulating orifices unchoke. A good window appears to be between 100 and 150 milliseconds for the MIT Stage compression system.

The supply tank pressure rate of change method appears to be a reliable method of continuous weightflow evaluation during the blowdown process. This does not depend on the one dimensional nature of the flow after the stage, and is thus applicable to runs in which stall cells appear.

MIT Transonic Compressor Stalled Flow Performance

(1) From the corrected weightflow and stall cell circumferential extent comparisons, it appears that stall cell extent does correlate well with flow blockage, with the part span stall cell responding with a definite time lag of approximately 1 rotor revolution to changes in weightflow.

(2) Comparisons with the Day, Greitzer, and Cumpsty correlation show that the MIT Transonic Stage's part span rotating stall flow pressure rise performance is somewhat lower than that of purely subsonic high hub-tip ratio stages.

(3) The part span stall cells exhibited in this stage appear to include large radial flows.

(4) An observation of transition from a single stall cell to two stall cells showed that succeeding stall cells can form in previously unstalled flow, rather than divide.

(5) Although the gross behavior of the unstalled flow is similar to operating conditions in which the stall cells did not exist, there are definite changes in the unstalled flow in relation to the stall cells.

(6) In the absolute frame, the flow is observed to have a higher axial component on the leading edge (unstalling side) than the trailing edge (stalling side) of the stall cell.

Suggestions for Future Work

As was pointed out previously, the existing radial traverse data was taken during a time interval in which the corrected weightflow was changing, and it would be desirable to have constant weightflow traverse data. Also, data should be taken behind the stator to provide a more complete picture of the flow field. Preferably, this should be done with a re-designed stator; the present stator appears to be badly mismatched.

Because traverse data is made with the probe at a fixed angle, and the probe has a limited useful flow acceptance angle, it seems to be necessary to repeat runs with the probe at varying preset angles. This is necessary since the flow angles between the stalled and unstalled flow can differ considerably.

The traverse flow data for this present work was reduced by hand from the analog signals, as the digitized version of these signals proved to be unsuitable for machine reduction, due to poor resolution. Thus, there are considerable possibilities for more detailed flow data from improved data reduction techniques. The requirement of using an ad hoc correction scheme, due to the probe thermal drift problem, is very unsatisfying, and could be

eliminated with improved instrumentation. However, the necessity for very fast response transducers, due to the limited test time of the blowdown process, combined with the violently transient nature of the blowdown process itself, makes the search for "improved instrumentation" understandably very difficult.

Finally, further study of the dynamic characteristics of the blowdown compression system would be worthwhile. This is especially true for stalled flow investigations, where operation on the positive sloped portion of the compressor characteristic makes oscillations in weightflow likely.

APPENDIX AWeightflow Calculation Uncertainty Using Analog Data

In this appendix, an analysis of the procedure used to find the weightflow using the analog data is presented. Measurement of this analog data is made on 17.8 cm. wide oscillograph strip charges as described in a previous section. The galvanometer light pens used have a sensitivity of about .24 volts per cm. so that the +/- 1.5 volt multiplex signal spreads over most of the width of the strip chart. (For this reason, more sensitive light pens could not be used to increase resolution.)

The Statham gauge on the supply tank has a sensitivity of approximately 90 kPascal (kPa) per volt*, so that the multiplex channel representing the supply tank has a chart sensitivity of about 20 kPa per cm. Since the pressure change in the supply tank is roughly 40 to 50 kPa during the tests, the chart change is about 2.5 cm.

The chart time scale is dependent, of course, on the playback and chart speed. For the multiplex signal, a scale factor of about 5 milliseconds per cm. results in a manageable chart length with discrete data points. Thus, assuming an achievable accuracy by hand, using a divider and scale of about 1/4 mm., the uncertainty in measured pressure is approximately .5 kPa, which is of the order of 1% of the test range of pressures. The time scale uncertainty is about

*1 atmosphere = 10^5 Pascal = 100 kPa.

.1 milliseconds, but can be made arbitrarily smaller by decreasing the playback speed and increasing the chart speed. 0.1 milliseconds is a quite adequate error margin for the time scales of interest here.

A simple analysis of the effects of this resolution on the calculation of the weightflow can be made using these values. The relationship for the blowdown weightflow evaluated from the rate of change of pressure in the supply tank has the following form:

$$W = K P^c \frac{\Delta P}{\Delta t}$$

where W is the weightflow, P is the pressure, t is time, K and C are constants, assumed to be known without error.

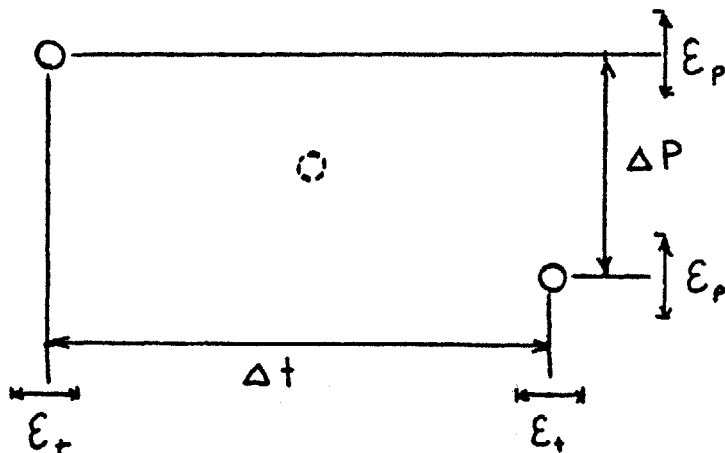
As measured, the terms P and t include error terms, ϵ_p and ϵ_t , respectively. P is the absolute value of pressure, and it is known that $\epsilon_p \ll P$, so the weightflow relationship can be simplified to

$$W = K' \frac{\Delta P}{\Delta t}$$

Expressed as uncertainty:

$$\delta(W) = K' \delta\left(\frac{\Delta P}{\Delta t}\right)$$

Consider the evaluation of the derivative in the neighborhood of any point, using a simple centered three point finite difference approximation.



The maximum uncertainty in $\frac{\Delta P}{\Delta t}$ expressed as the largest possible difference is:

$$\delta \left(\frac{\Delta P}{\Delta t} \right)_{\text{MAX}} = \frac{\Delta P + \epsilon_p}{\Delta t - \epsilon_t} - \frac{\Delta P - \epsilon_p}{\Delta t + \epsilon_t} = \frac{2\Delta t \epsilon_p + 2\Delta P \epsilon_t}{\Delta t^2 - \epsilon_t^2}$$

On the time scale of interest, $\epsilon_t^2 \ll \Delta t^2$, and can be neglected. Also dividing by $\frac{\Delta P}{\Delta t}$,

$$\frac{\delta \left(\frac{\Delta P}{\Delta t} \right)_{\text{MAX}}}{\Delta P / \Delta t} = \frac{2 \epsilon_p}{\Delta P} + \frac{2 \epsilon_t}{\Delta t}$$

or finally

$$\frac{\delta(W)}{W} = \frac{2 \epsilon_p}{\Delta P} + \frac{2 \epsilon_t}{\Delta t}$$

On the scale of interest, the uncertainty in the time measurement is less than 1%. However, ΔP during approximately 20 milliseconds (as an example) can be of the order of 5 kPa. With ϵ_p of the order .5 kPa, the uncertainty in weightflow using the simple three point finite difference approximation can be as high as 20%, given the 1% accuracy of the strip chart data, and even higher for a shorter time. This error is unacceptable, and even if this simple analysis is not precisely correct, it is adequate to indicate that other methods must be sought for weightflow evaluation.

APPENDIX BFORAN Results: Samples

The following figures are examples of the results of the filtering routine FORAN.

Figure B1 is a plot of the results of MPLEX, showing the demultiplexed signal with the superimposed 120 Hz noise.

Figure B2 is a plot of the frequency/amplitude spectrum of this data interval, as analyzed by FORAN1.

Figure B3 is a plot of the original data interval reconstructed from the Fourier coefficients found by FORAN1. Only the first 100 coefficients were used. The high frequency large amplitude components are a result of the interpolation of the discrete data points, and are not "real."

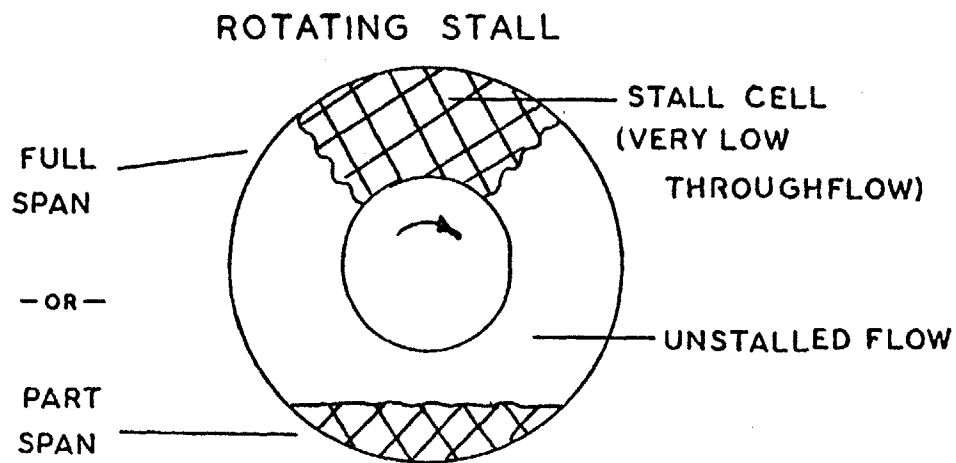
Figure B4 is a plot of the reconstructed data interval with the 120 Hz noise filtered out.

ACKNOWLEDGMENT

The authors would like to acknowledge Professor W. T. Thompkins for helpful discussions and Mr. Jose Converti for the probe placement scheme shown in Figure 4.

REFERENCES

1. Kerrebrock, J. L., "The M.I.T. Blowdown Compressor Facility," GTL Report No. 108, Gas Turbine Laboratory, M.I.T., May 1972.
2. Epstein, A. H., "Quantitative Density Visualization in a Transonic Compressor Rotor," GTL Report No. 124, Gas Turbine Laboratory, M.I.T., September 1975.
3. Thompkins, W. T., "An Experimental and Computational Study of the Flow in a Transonic Compressor Rotor," GTL Report No. 129, Gas Turbine Laboratory, M.I.T., May 1976.
4. Farokhi, S., "Unsteady Flow in a Transonic Compressor Stage," M.S. Thesis, M.I.T. Department of Aeronautics and Astronautics, May 1976.
5. Figueiredo, W., "Mean Flow Measurements of the Blowdown Transonic Stage," M.S. Thesis, M.I.T. Department of Aeronautics and Astronautics, May 1978.
6. Figueiredo, W., "Spherical Pressure Probe for Retrieving Freestream Pressure and Directional Data," GT & PDL Report No. 137, Gas Turbine and Plasma Dynamics Laboratory, M.I.T., August 1977.
7. Day, I.J., E.M. Greitzer, and N.A. Cumpsty, "Prediction of Compressor Performance in Rotating Stall," ASME Paper No. 77-GT-10, December 1976.
8. Greitzer, E. M., "Surge and Rotating Stall in Axial Flow Compressors, Part 1: Theoretical Compression System Model," ASME Paper No. 75-GT-9, November 1974.
9. Day, I. J. and N. A. Cumpsty, "The Measurement and Interpretation of Flow Within Rotating Stall Cells of Axial Compressors," University of Cambridge, Report CUED/A-Turbo/TR 90, 1977.
10. Kerrebrock, J. L., "Small Disturbances in Turbomachine Annuli with Swirl," AIAA Journal, Vol. 15, No. 6, June 1977, pp. 794-803.



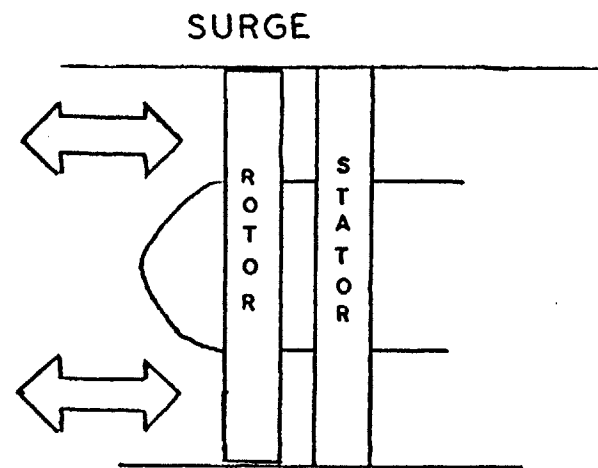
CIRCUMFERENTIALLY NONUNIFORM FLOW

STALL CELL PROPOGATES RELATIVE TO ROTOR, AT TYPICALLY HALF ROTOR SPEED

ONE OR MORE STALL CELLS

ANNULUS AVERAGED THROUGHFLOW IS CONSTANT

MAY APPEAR AS EITHER FULL SPAN OR PART SPAN STALL

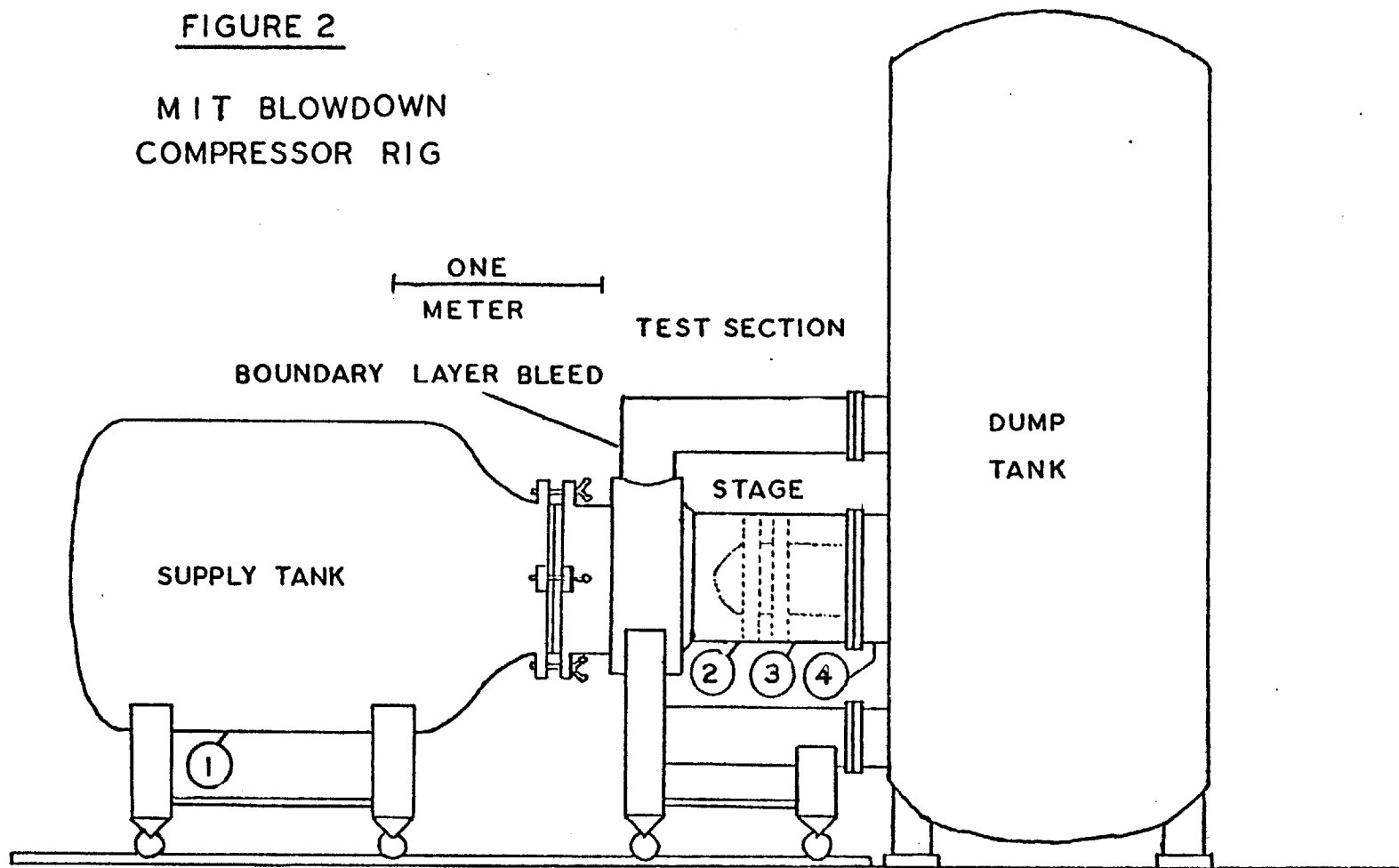


OSCILLATIONS IN ANNULUS AVERAGED THROUGHFLOW

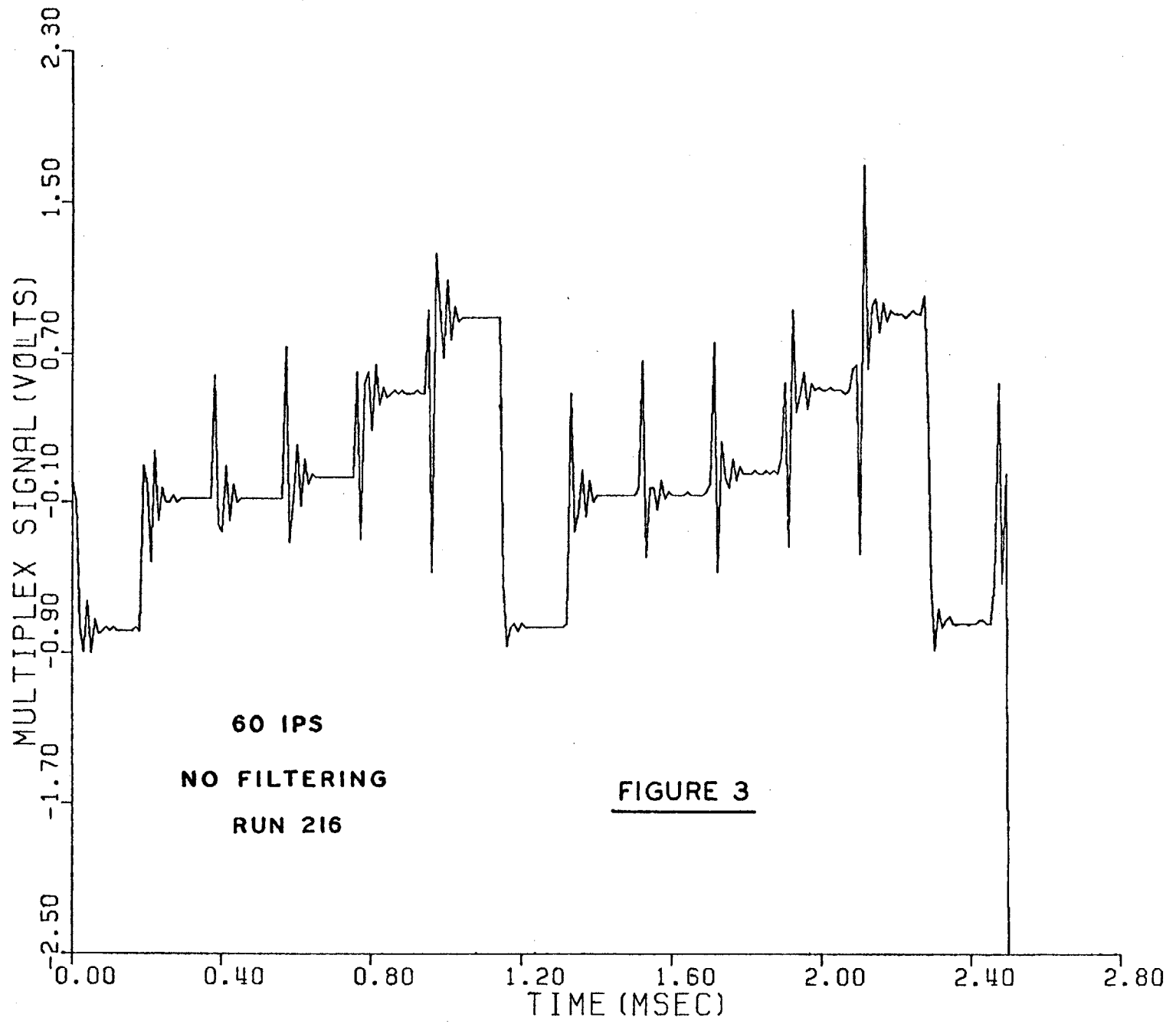
GENERALLY, MUCH LOWER FREQUENCY DISTURBANCE THAN CHARACTERISTIC OF ROTATING STALL CELLS

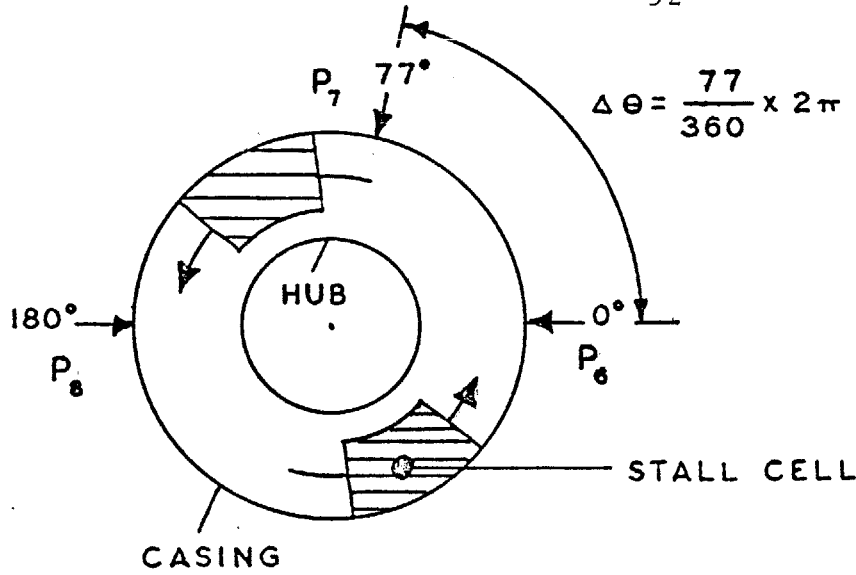
FIGURE 1

FIGURE 2
MIT BLOWDOWN
COMPRESSOR RIG

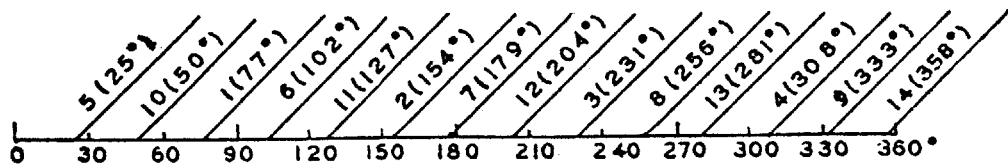
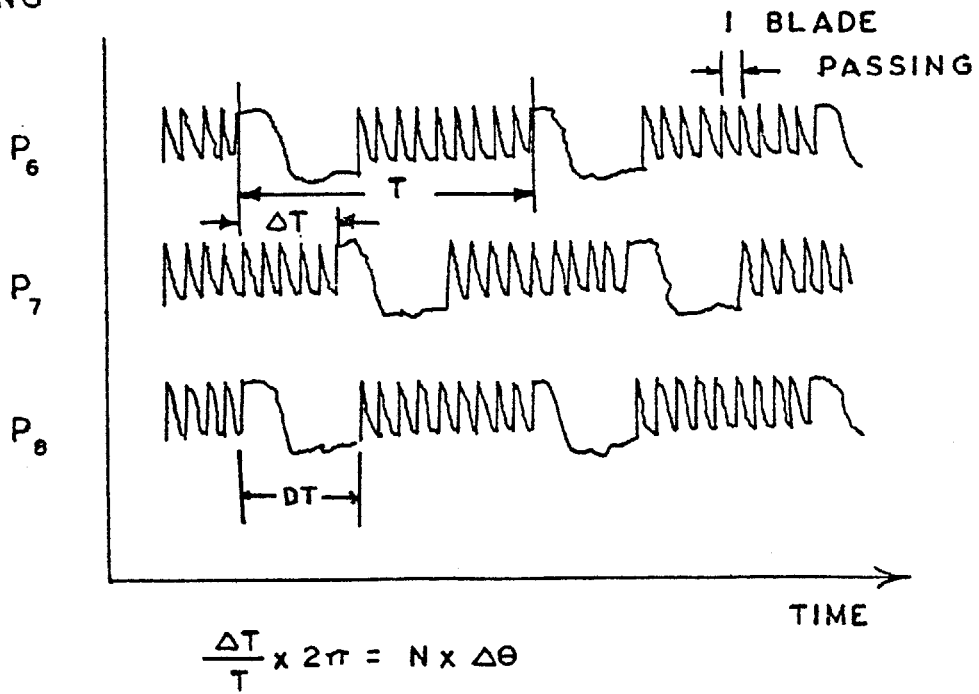


① ② ③ ④ — LOCATION OF PRESSURE TRANSDUCERS
(HIGH FREQ. TRANS. CIRCUMFERENTIALLY AT ②)





RELATIVE POSITION OF HIGH FREQUENCY WALL STATIC PRESSURE TRANSDUCERS



NUMBER OF STALL CELLS AS FUNCTION OF $\frac{\Delta T}{T}$

FIGURE 4

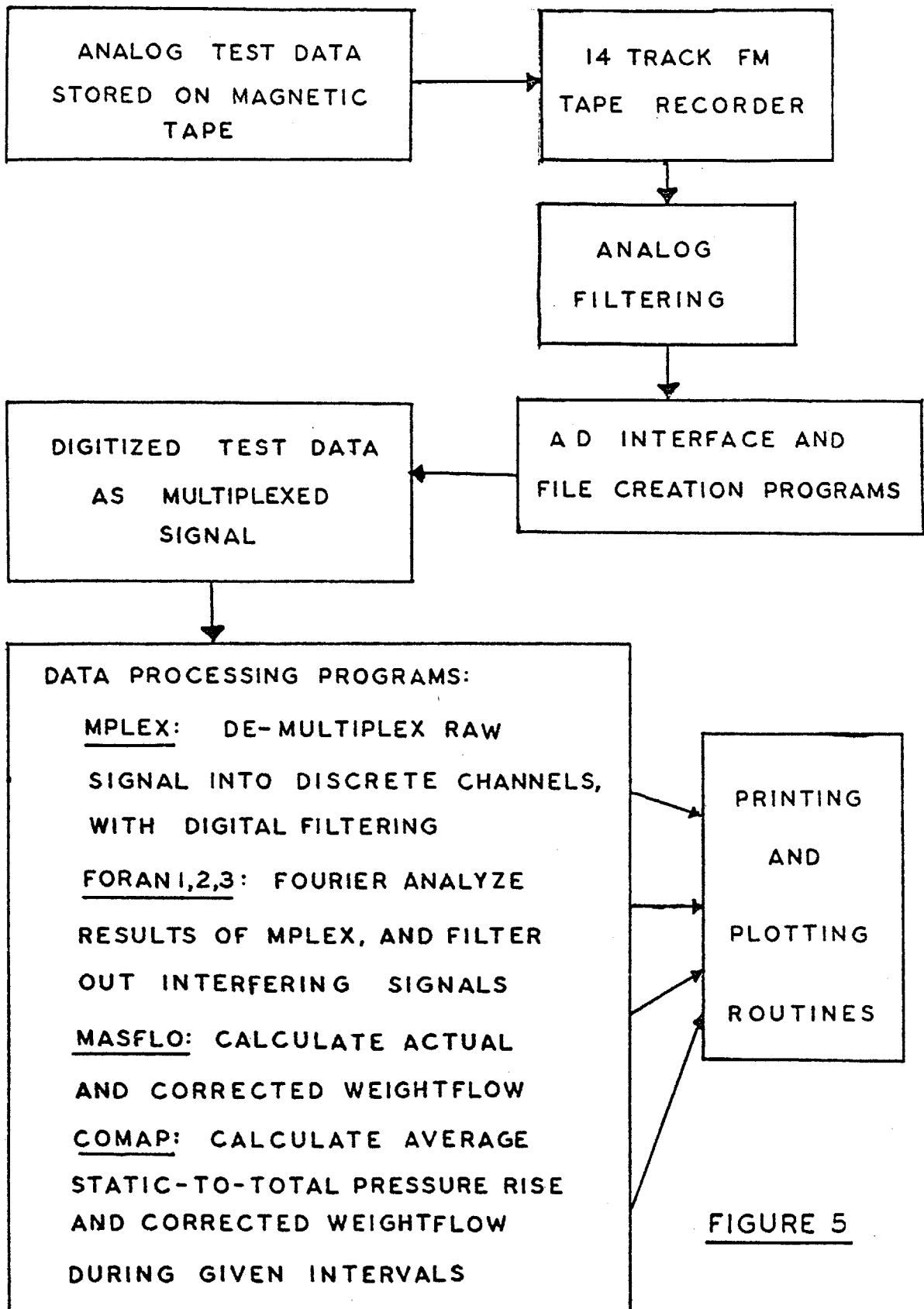
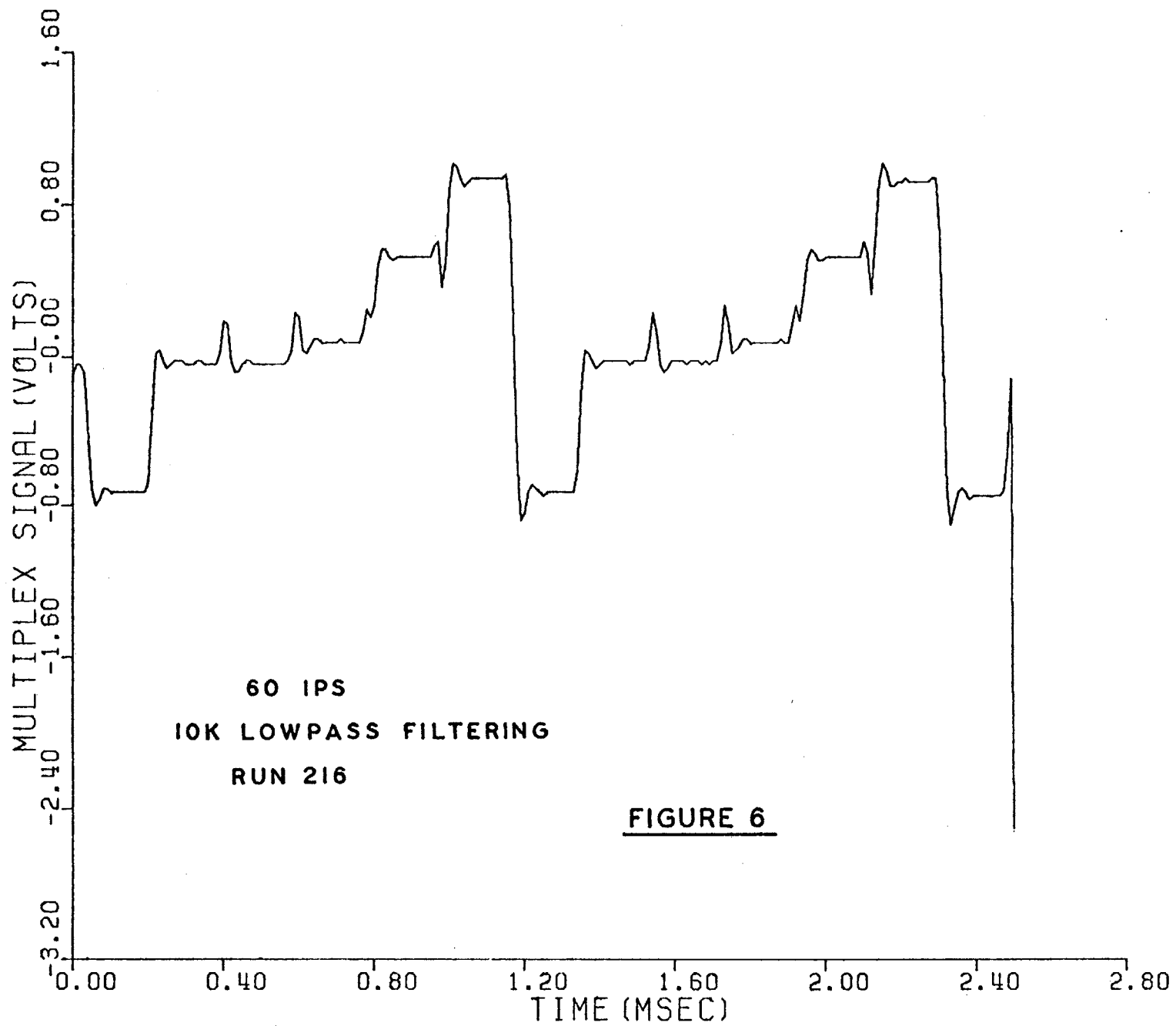
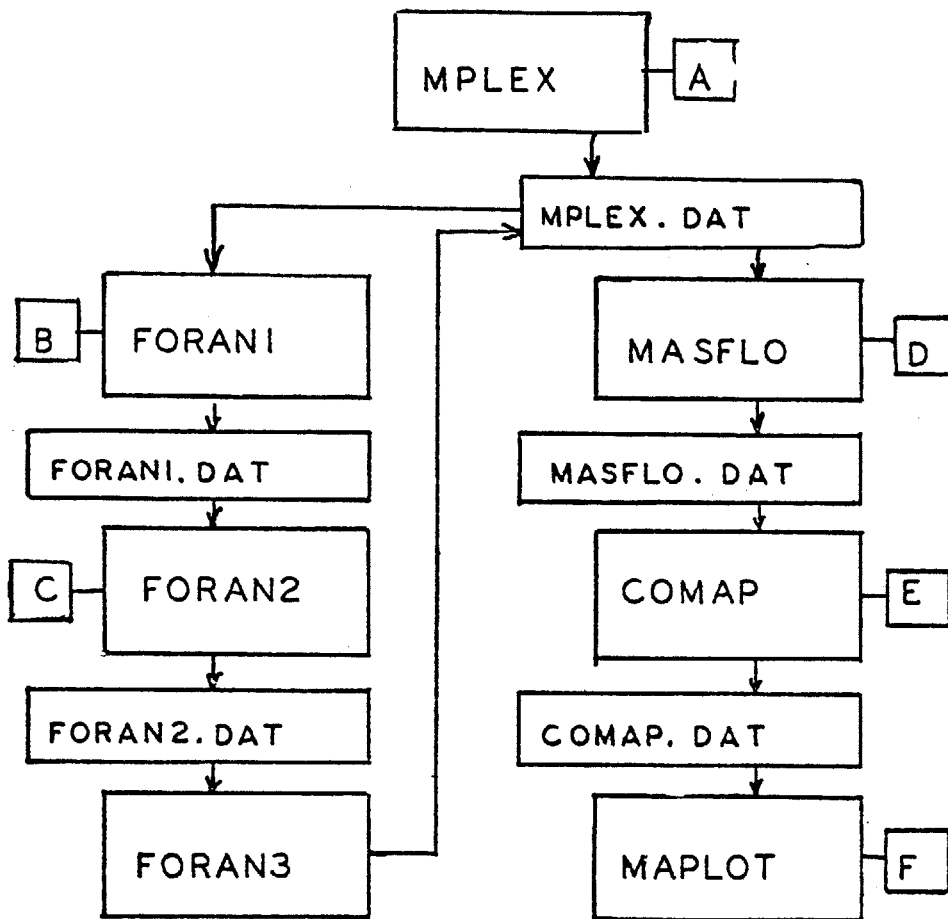




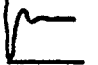



FIGURE 5



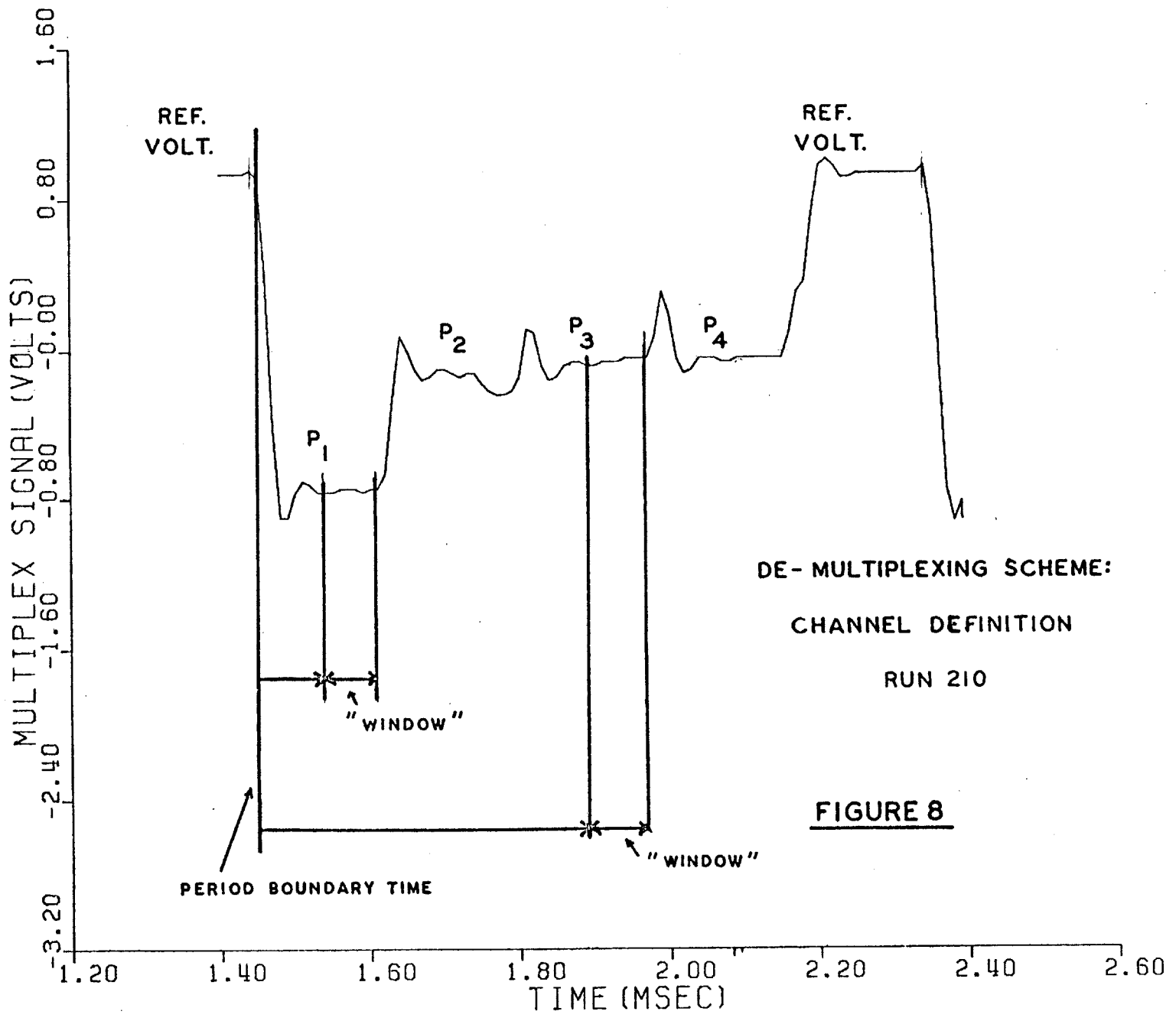
OUTLINE OF DATA REDUCTION PROGRAMS

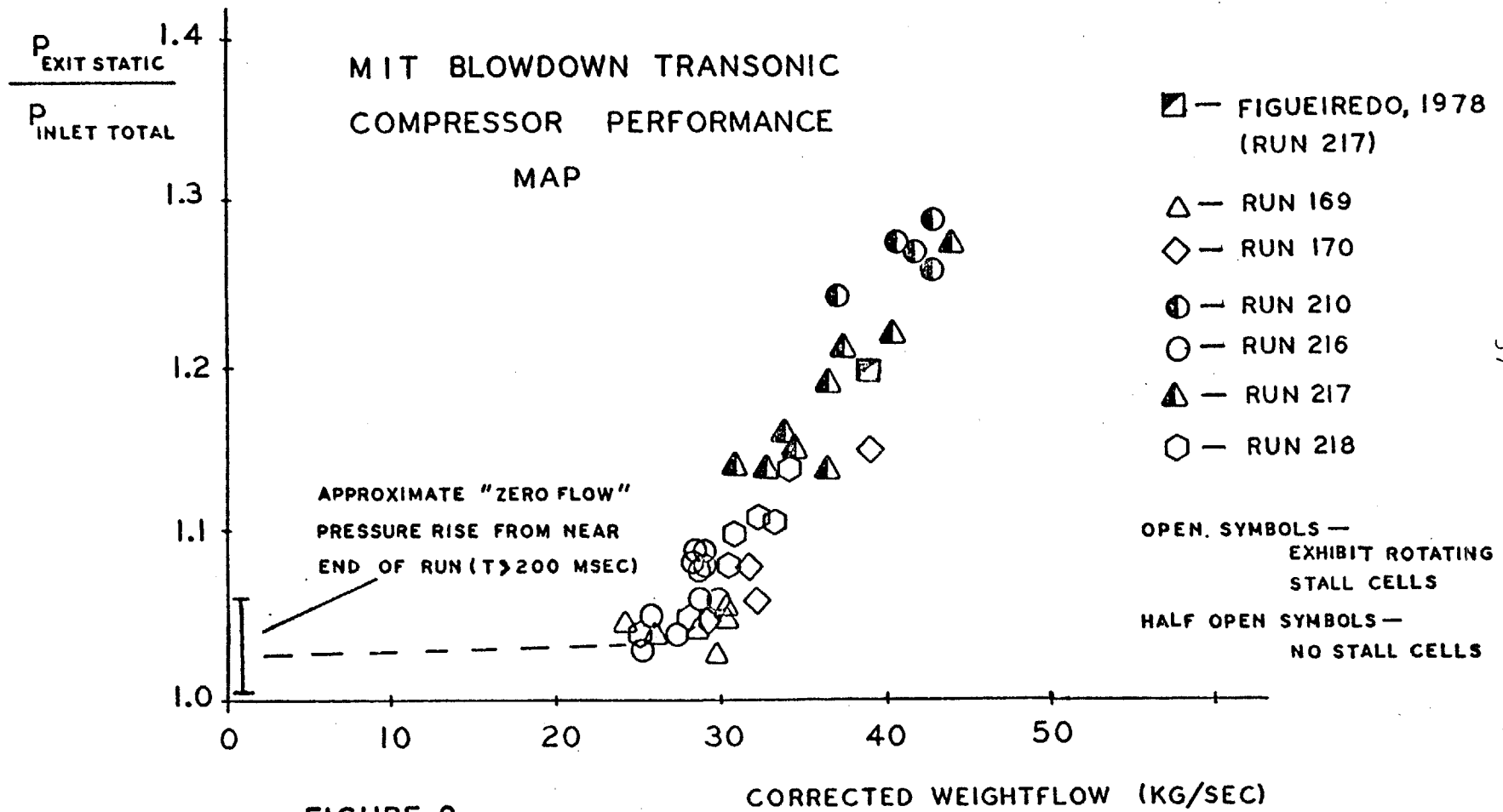


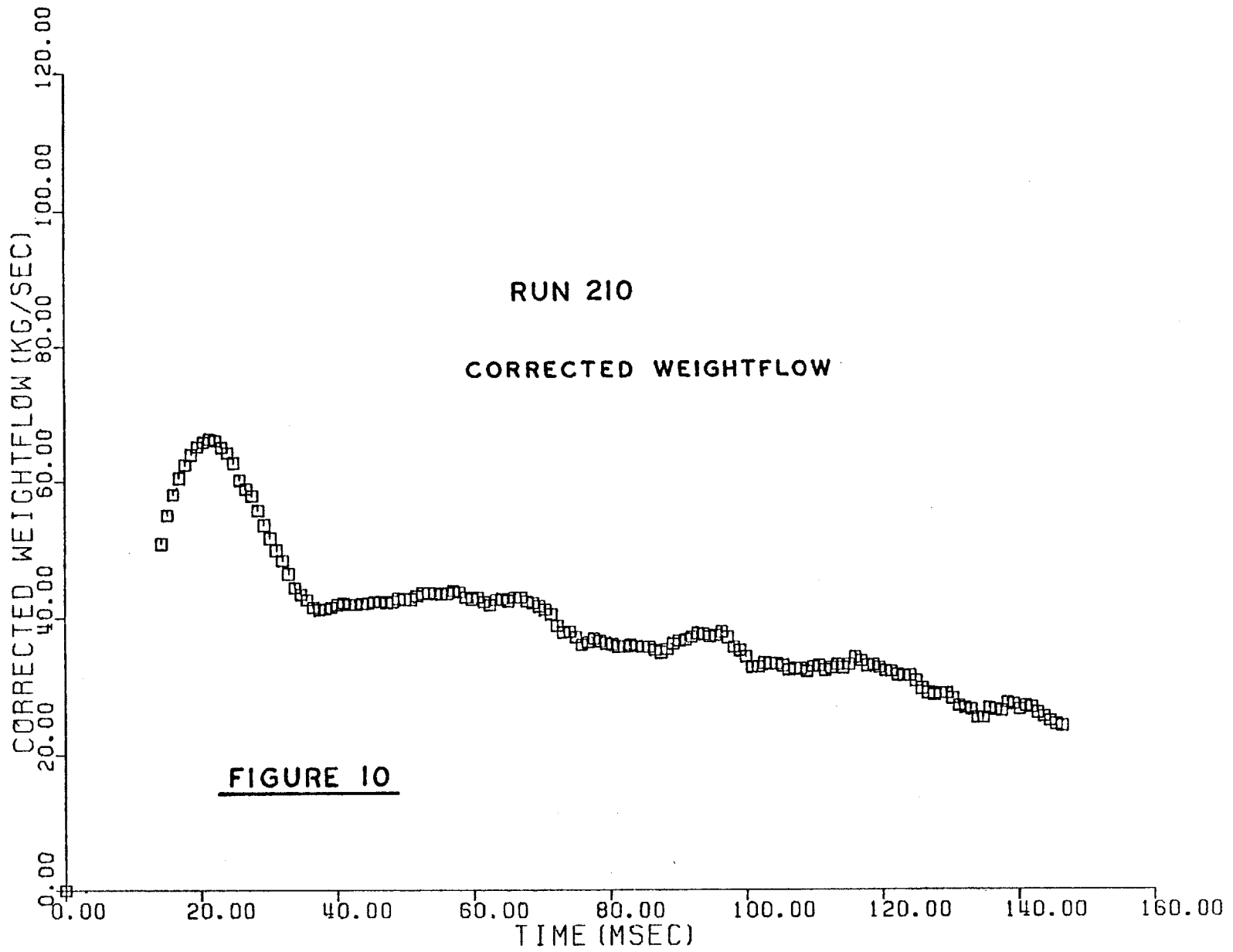
<p>A</p>  <p>DE - MULTIPLEXED CHANNELS</p>	<p>B</p>  <p>FREQUENCY/AMPLITUDE SPECTRUM AND RECONSTRUCTED CHANNELS</p>	<p>C</p>  <p>FILTERED RECONSTRUCTED CHANNELS</p>
<p>D</p>  <p>ACTUAL AND CORRECTED WEIGHTFLOW</p>	<p>E</p>  <p>STATIC-TO-TOTAL PRESSURE RISE</p>	<p>F</p>  <p>COMPRESSOR PERFORMANCE MAP</p>

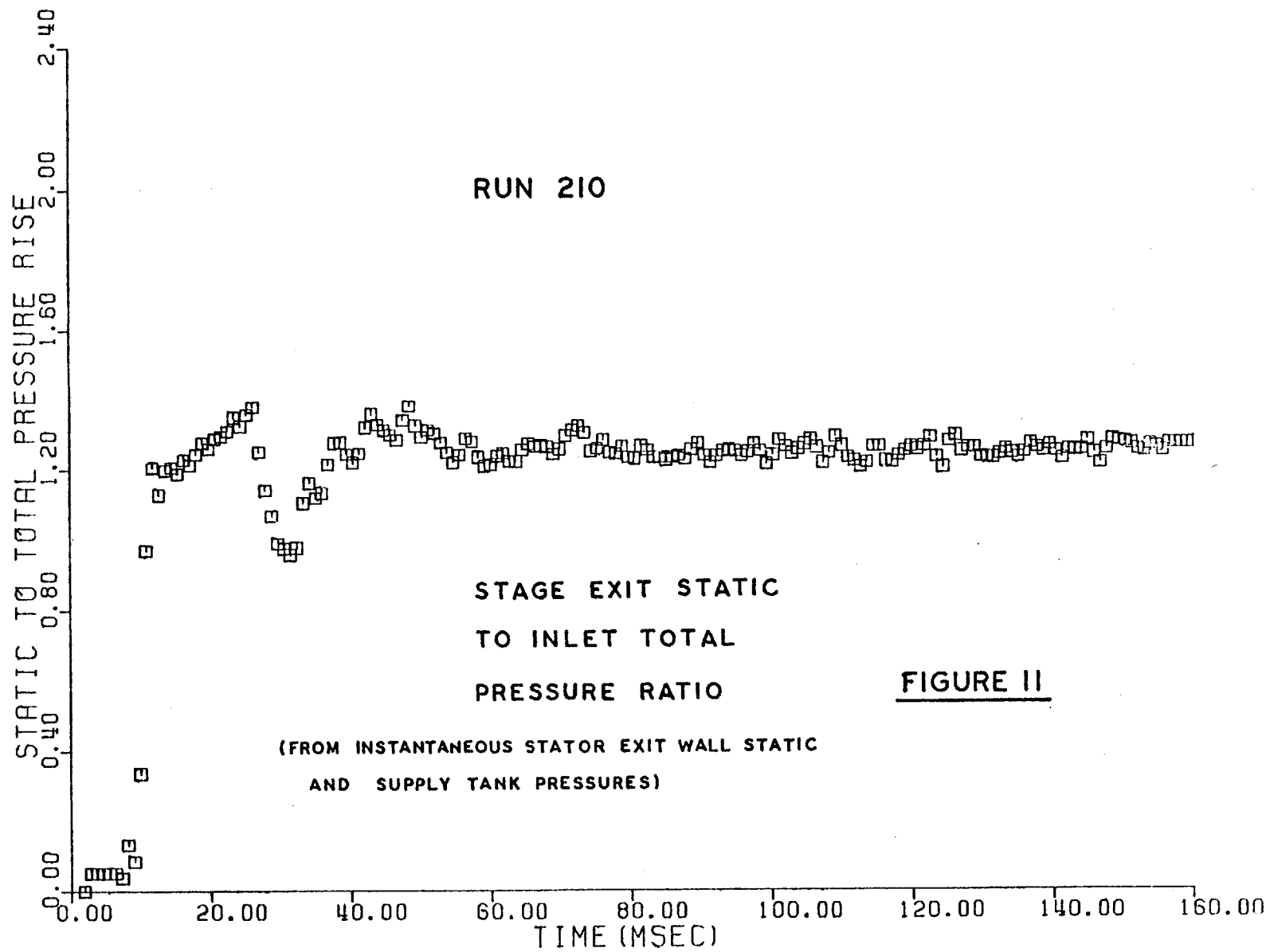
OUTPUT TABLE

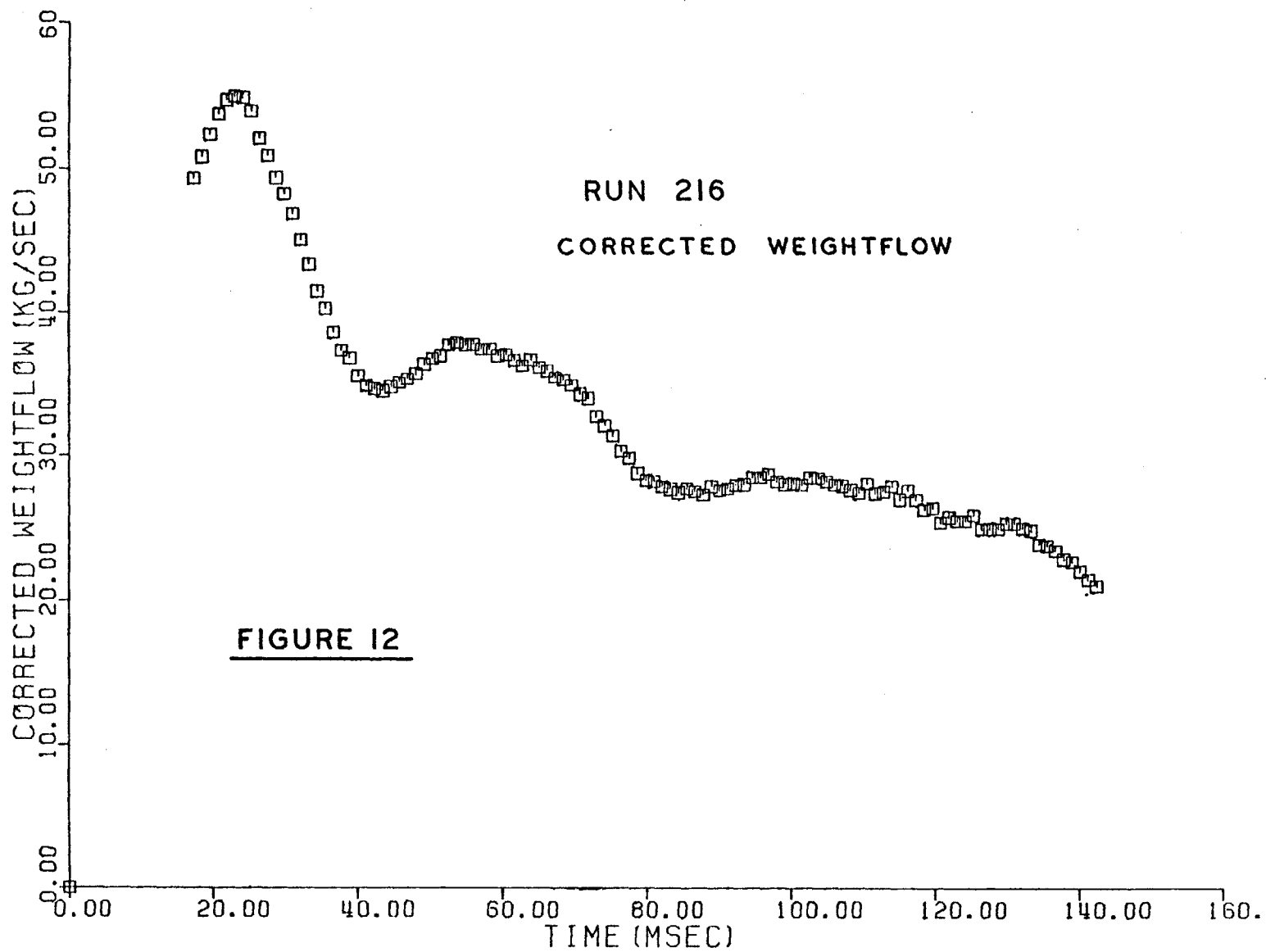
FIGURE 7

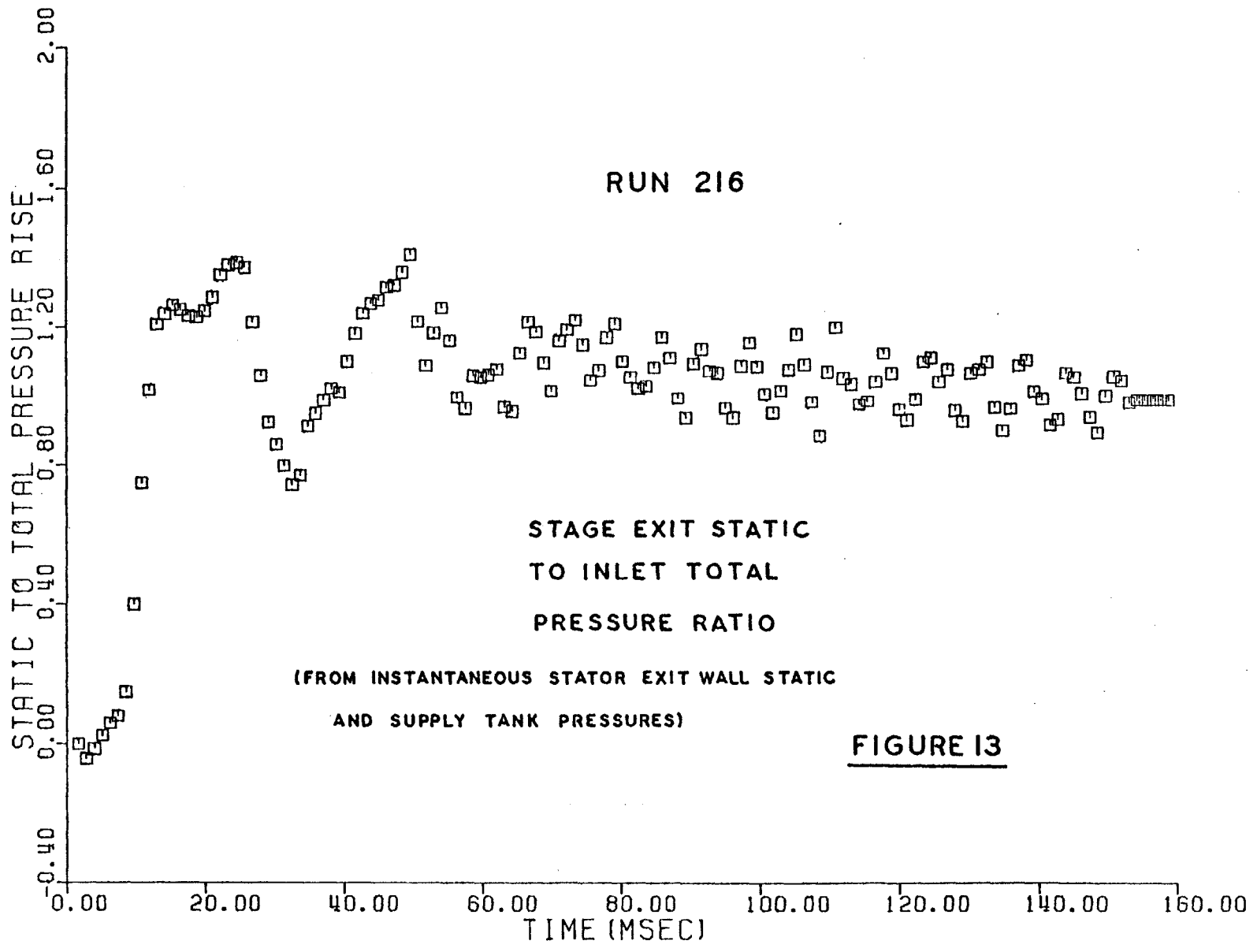


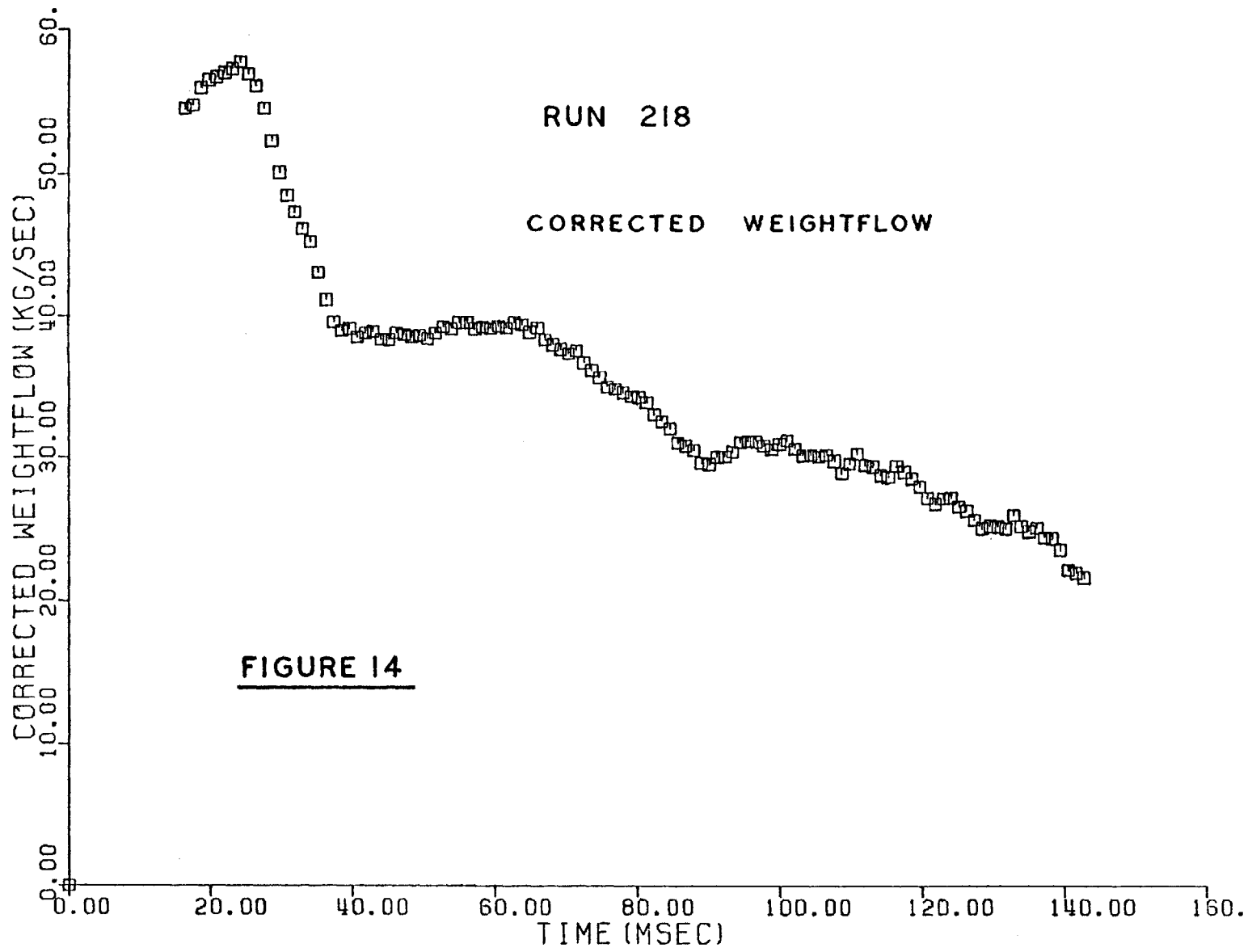


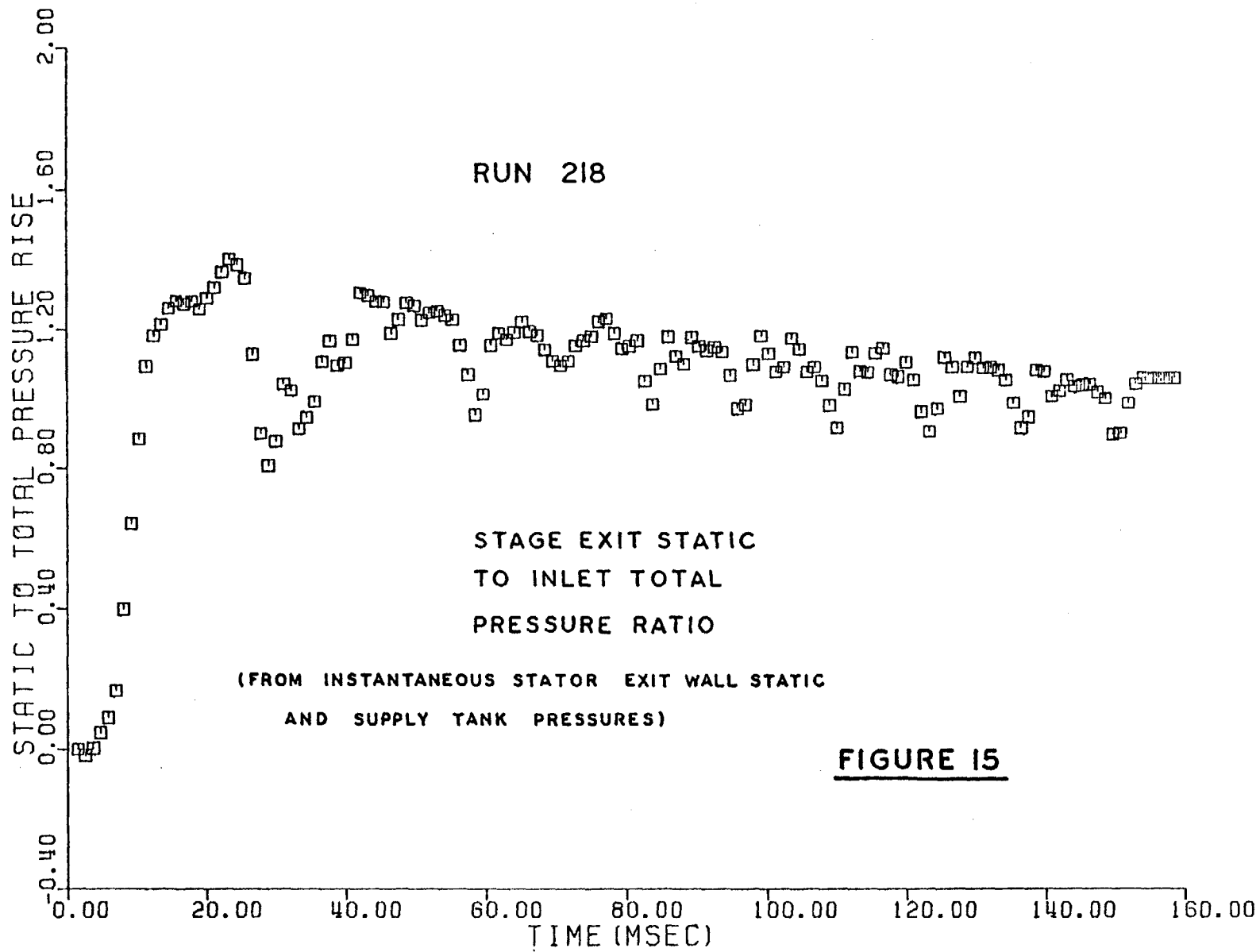












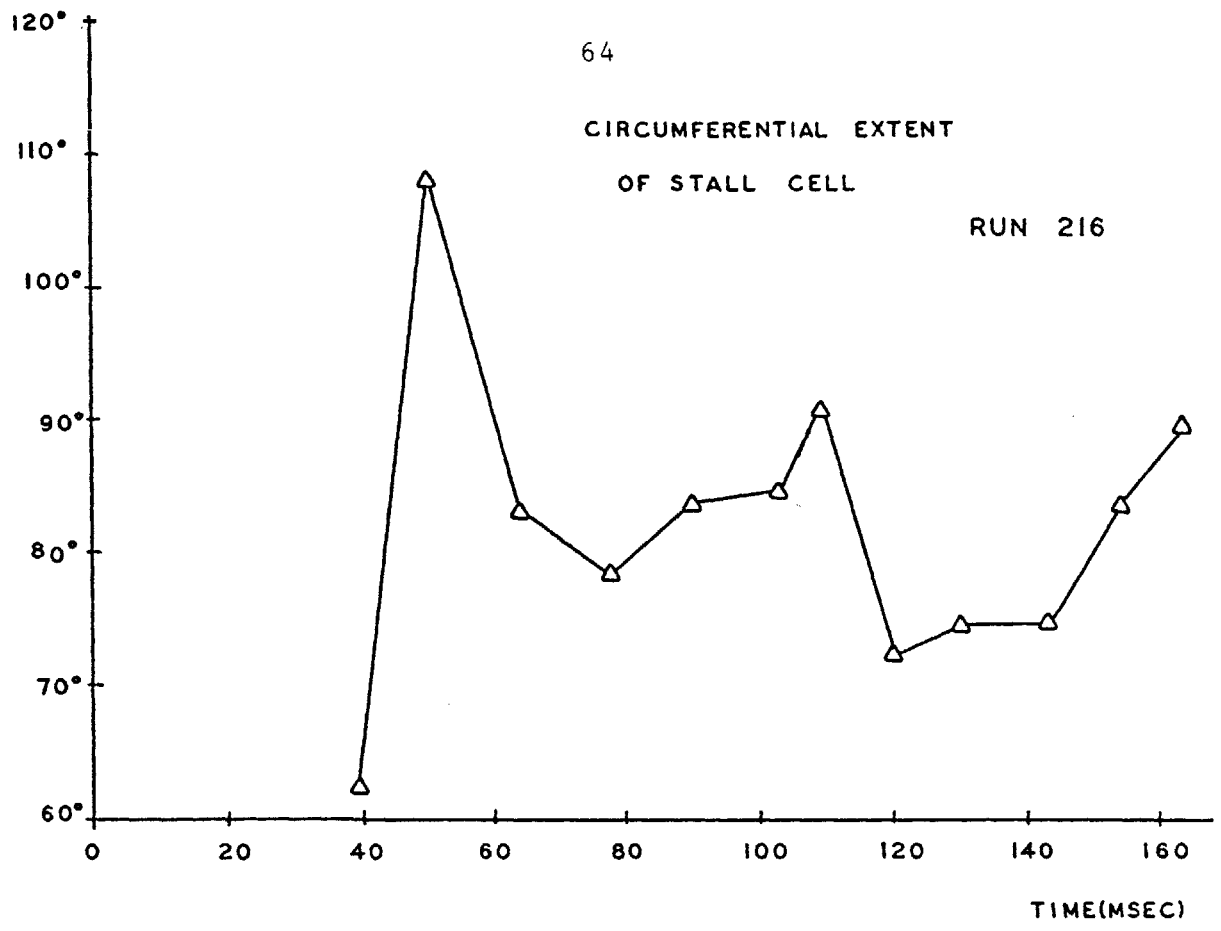
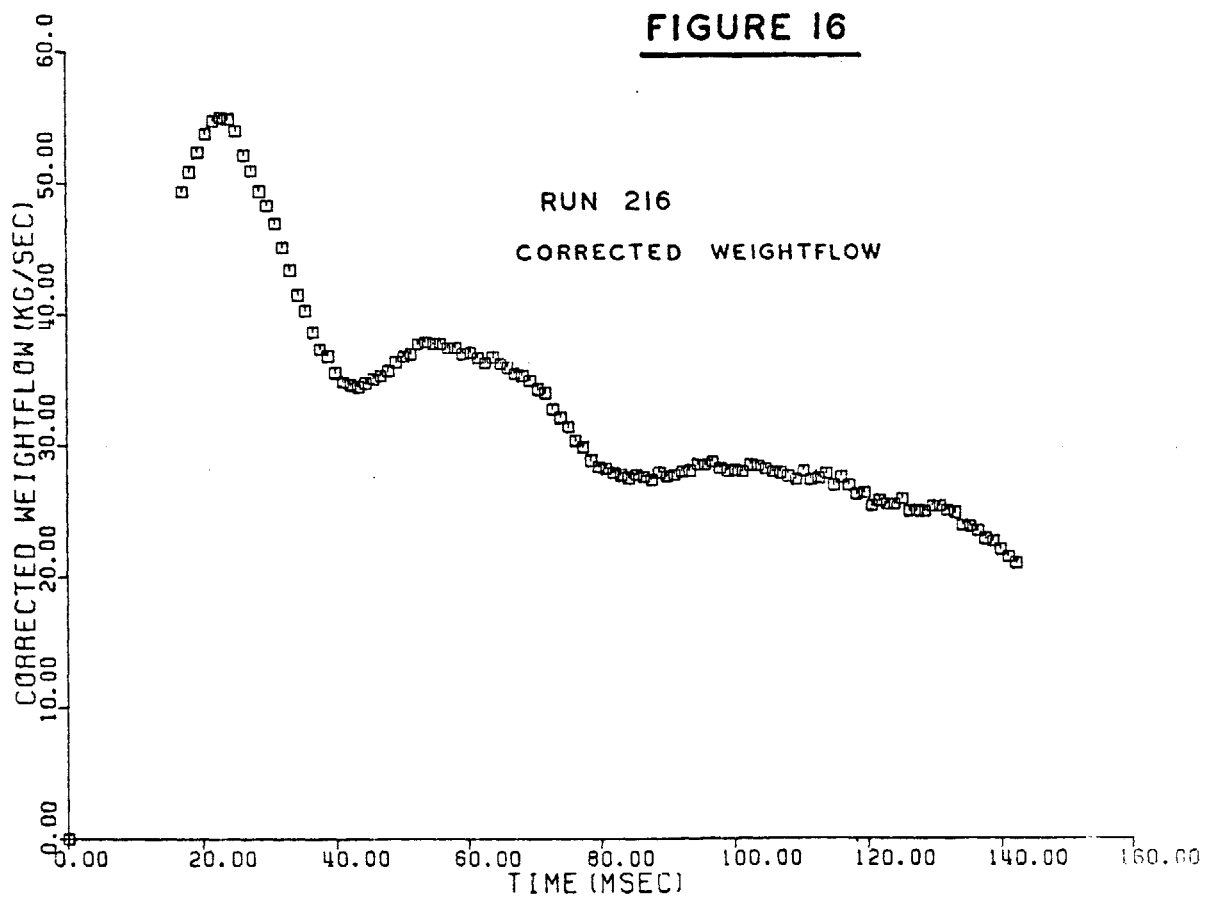


FIGURE 16



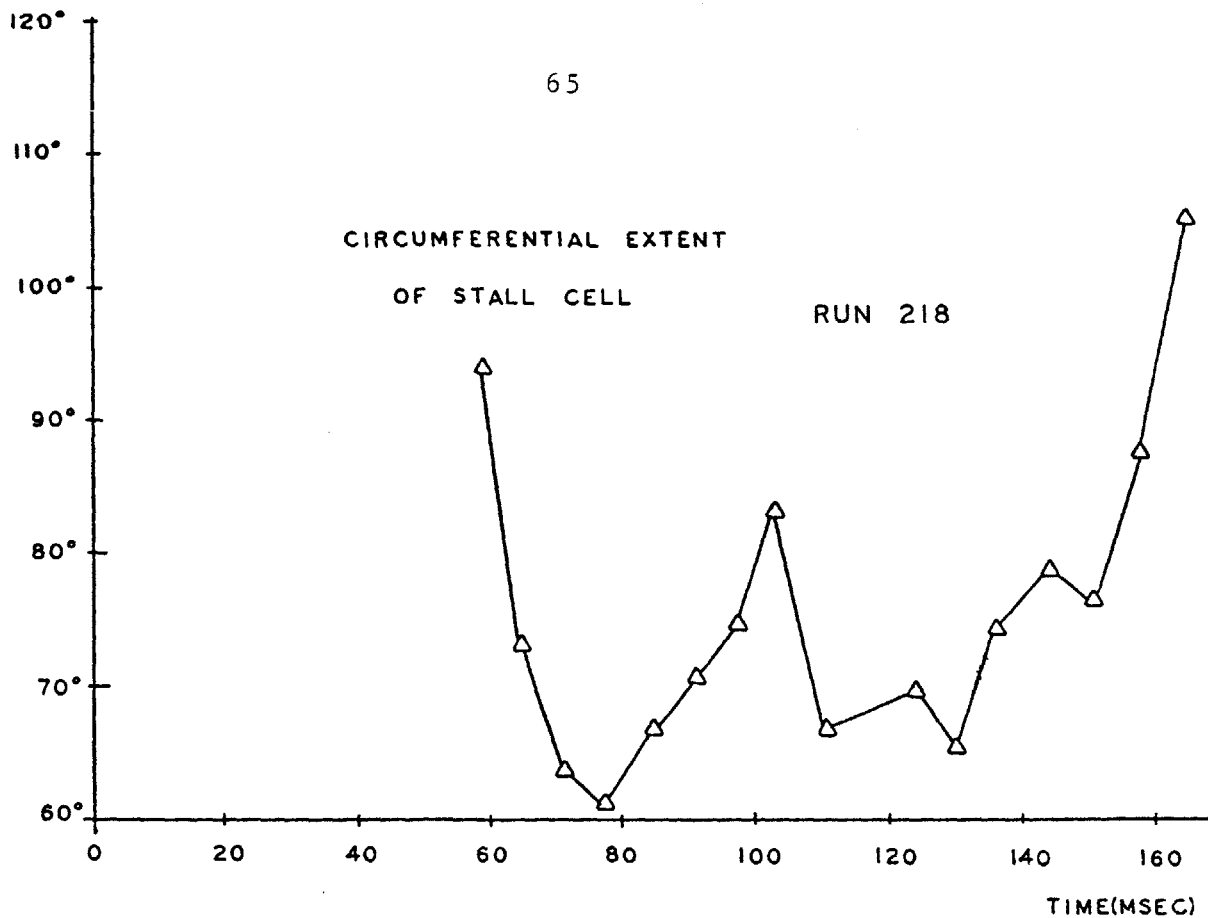
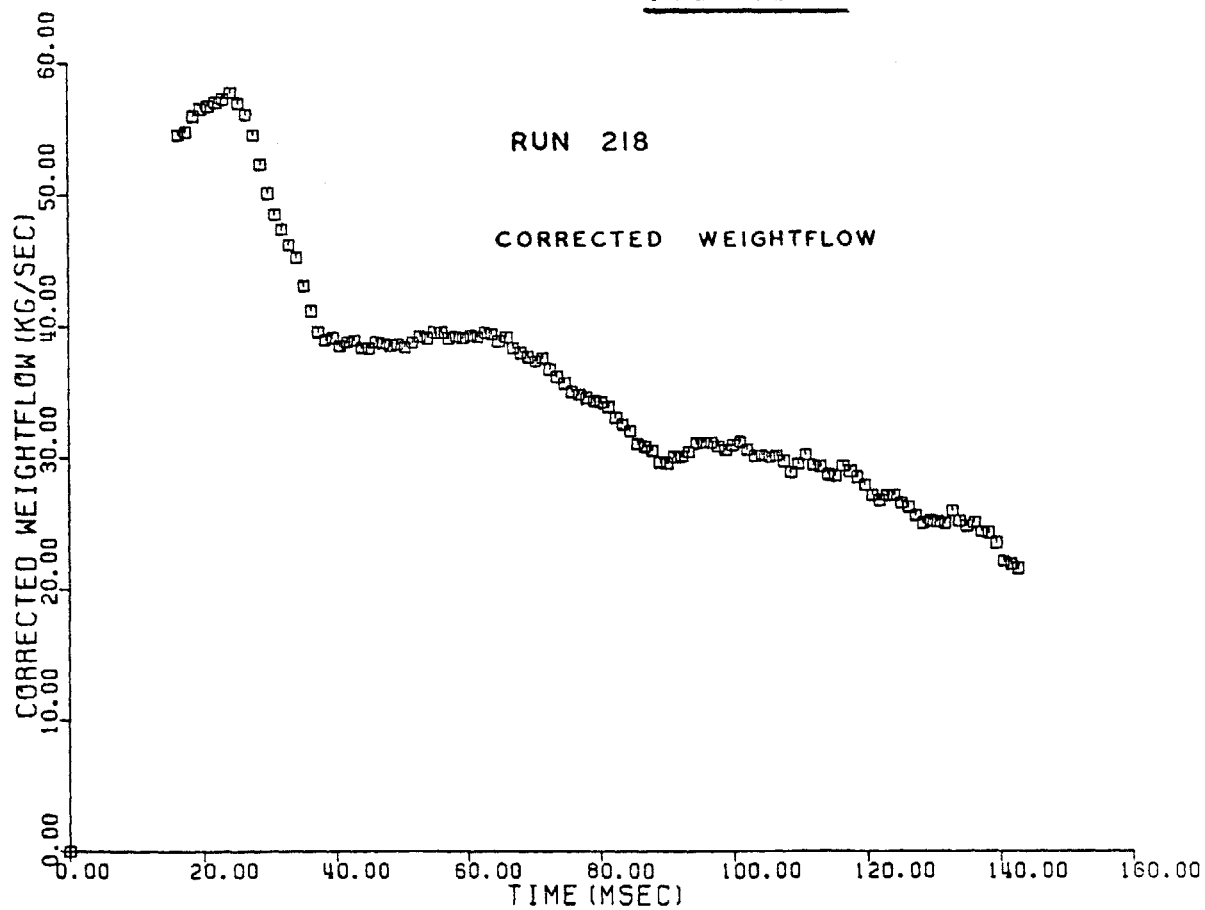
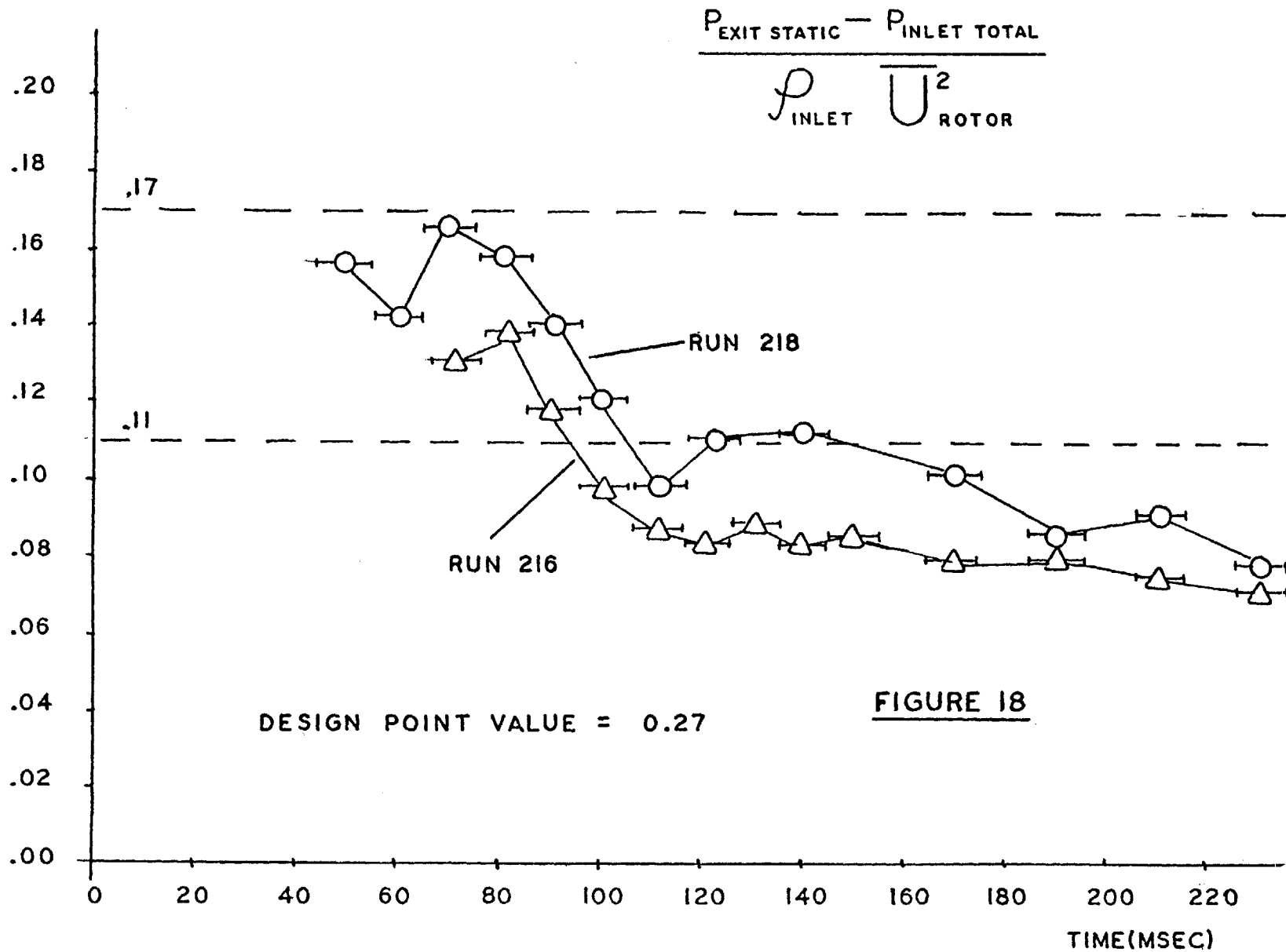
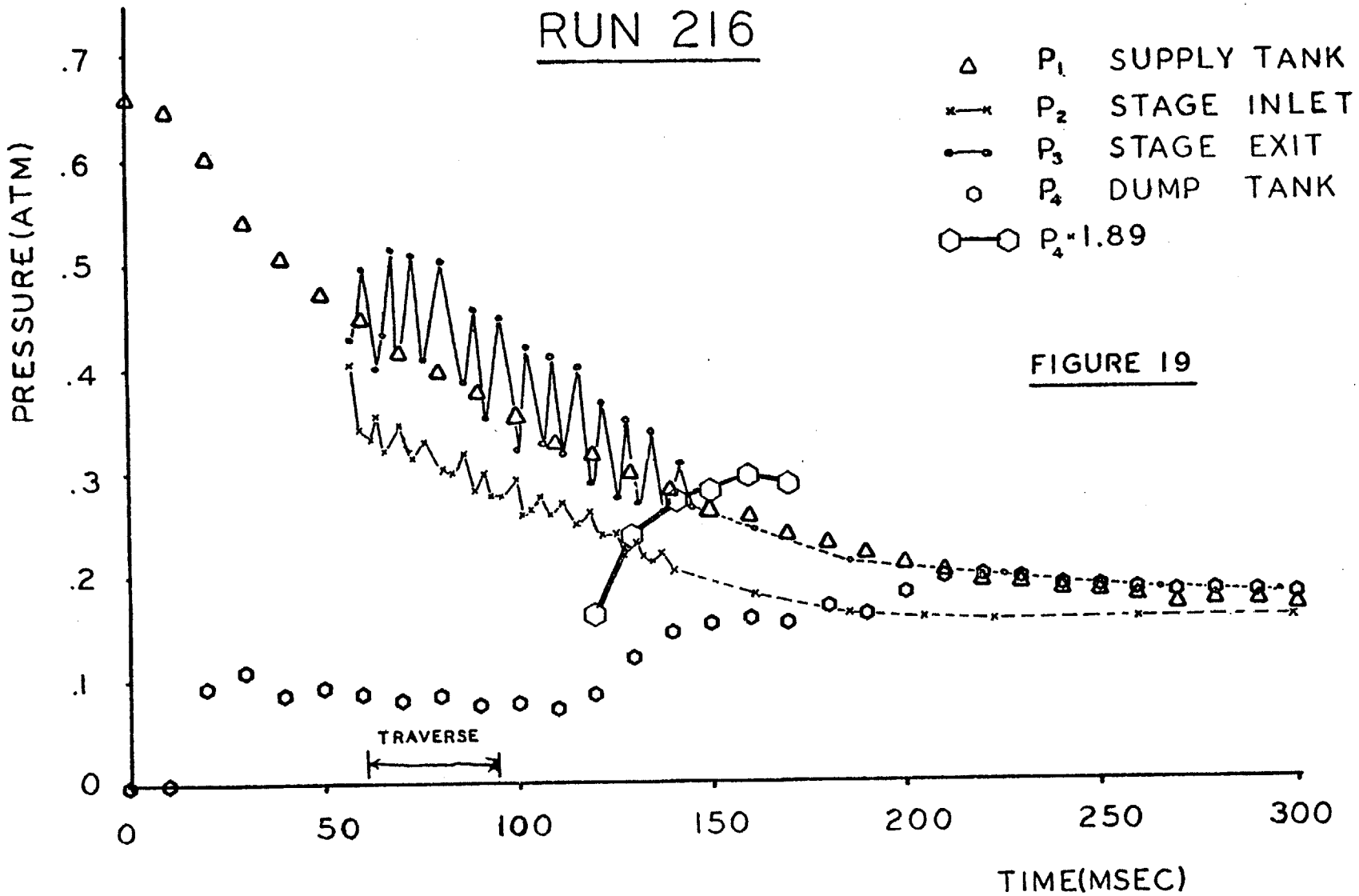


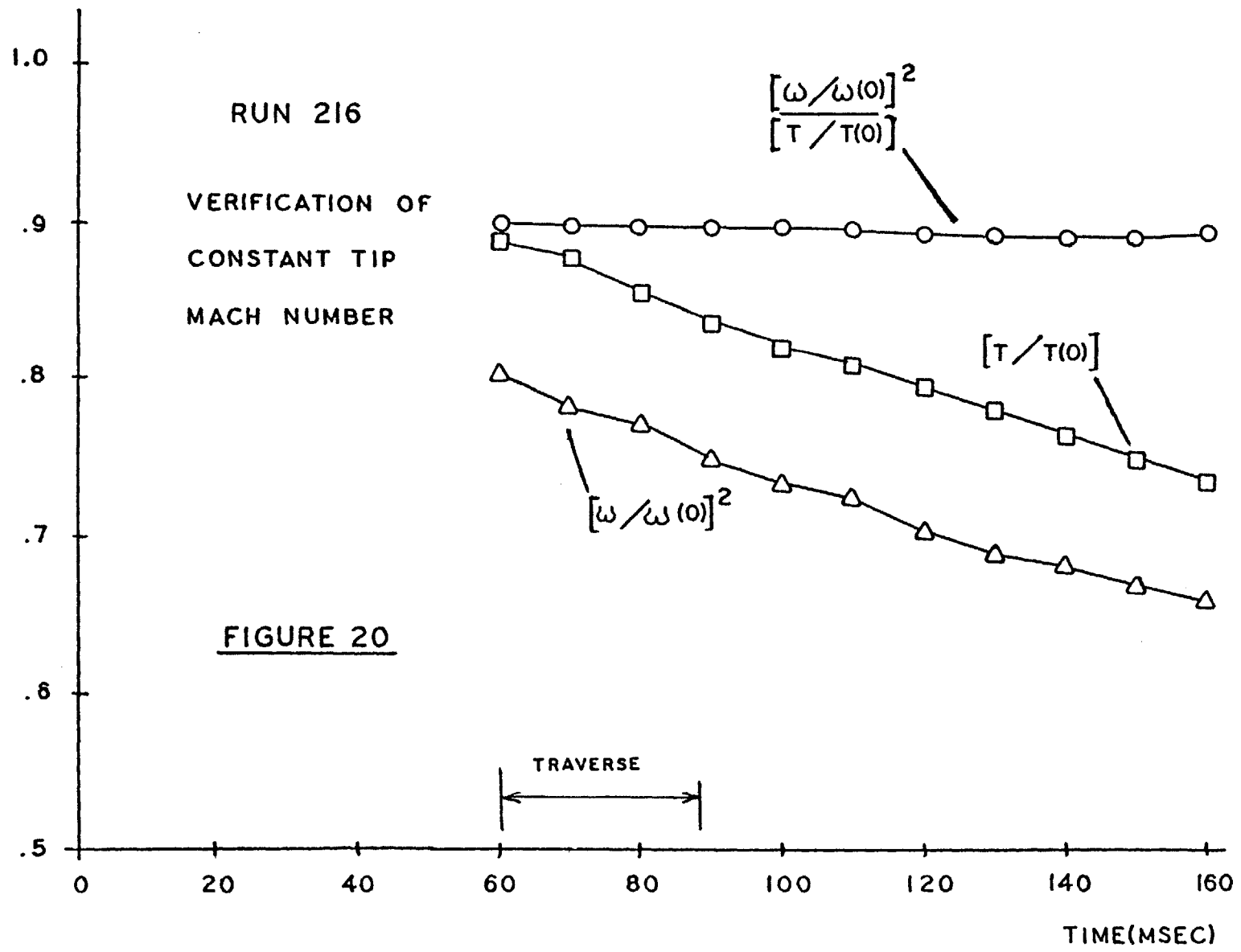
FIGURE 17

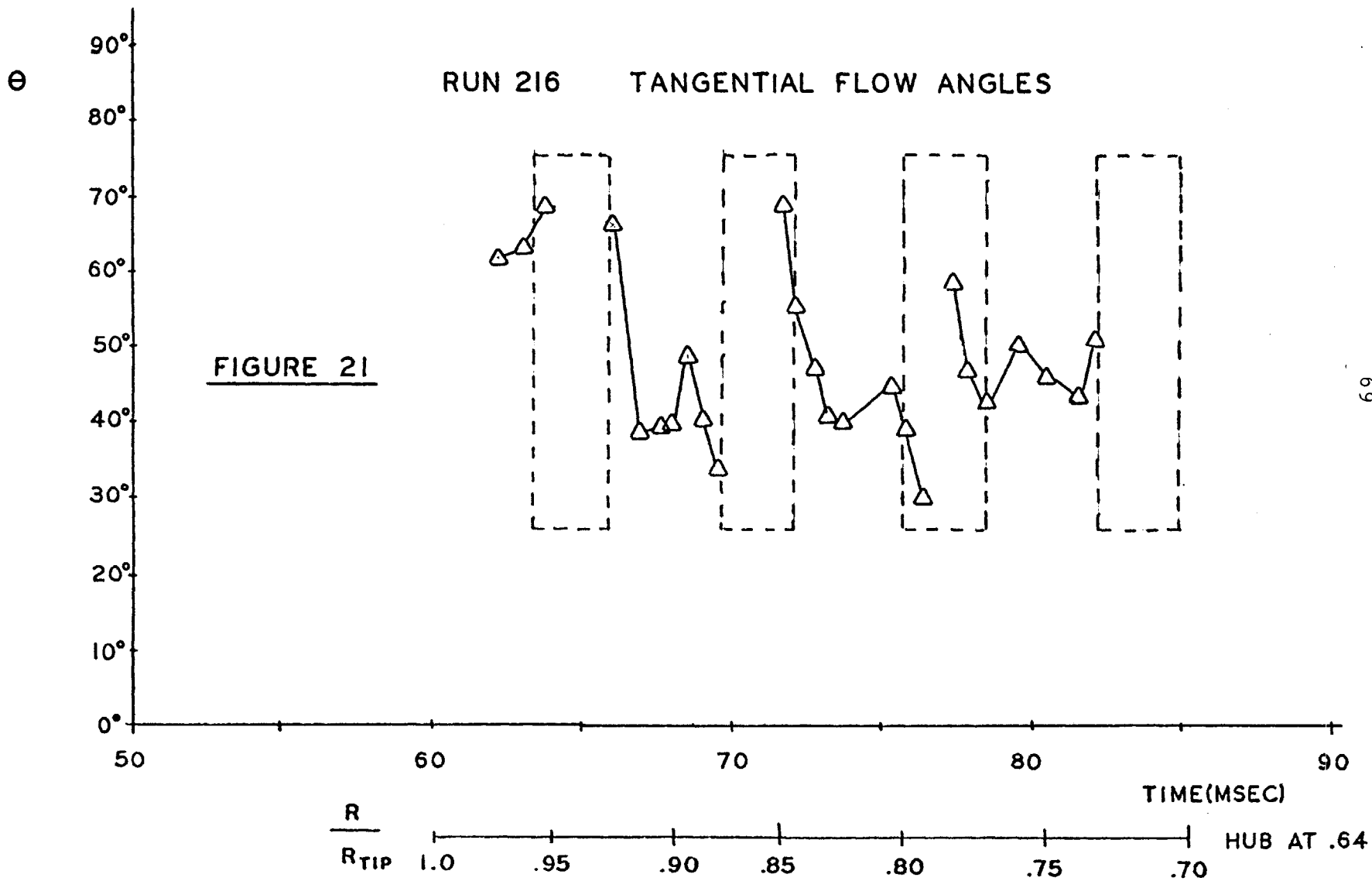


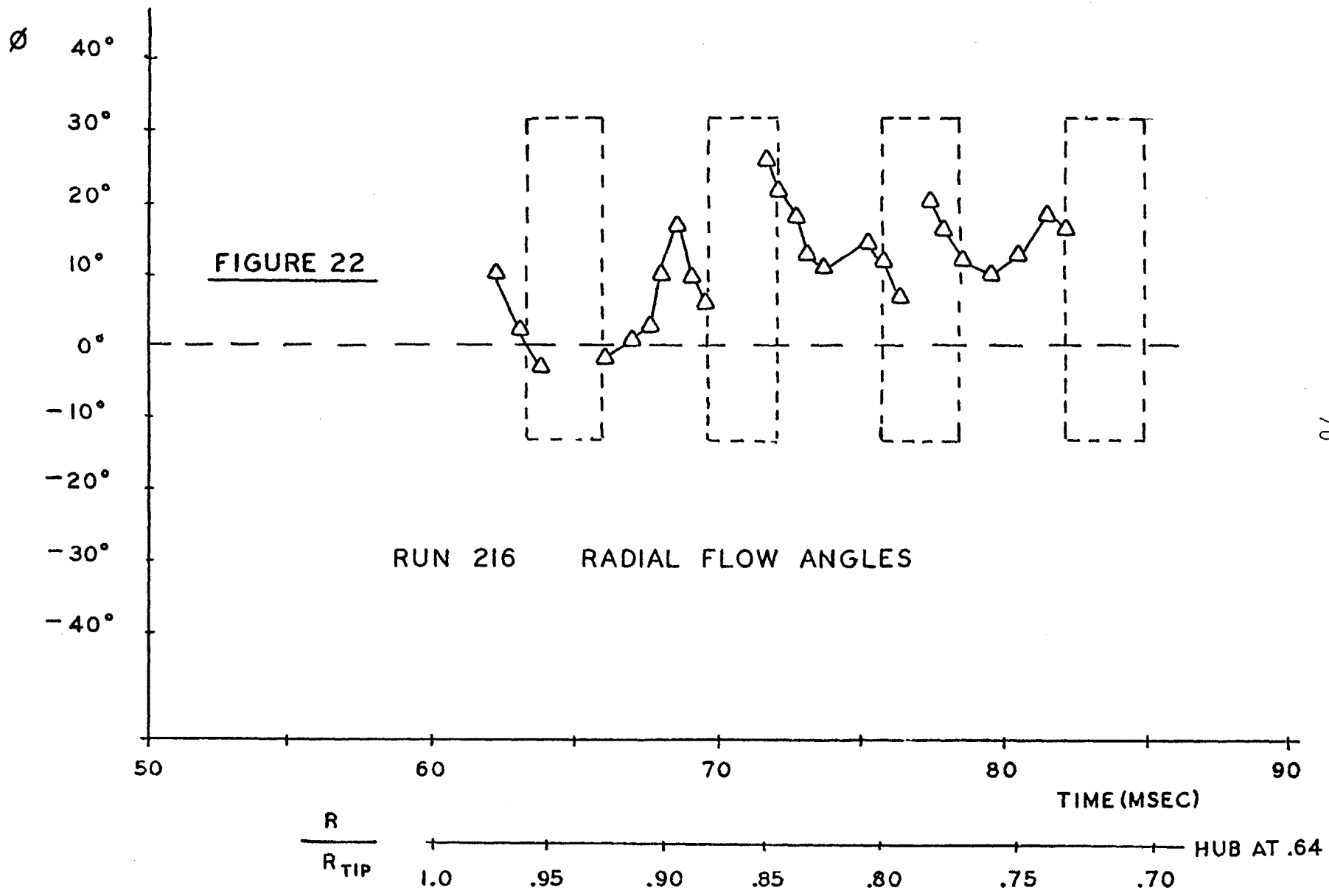


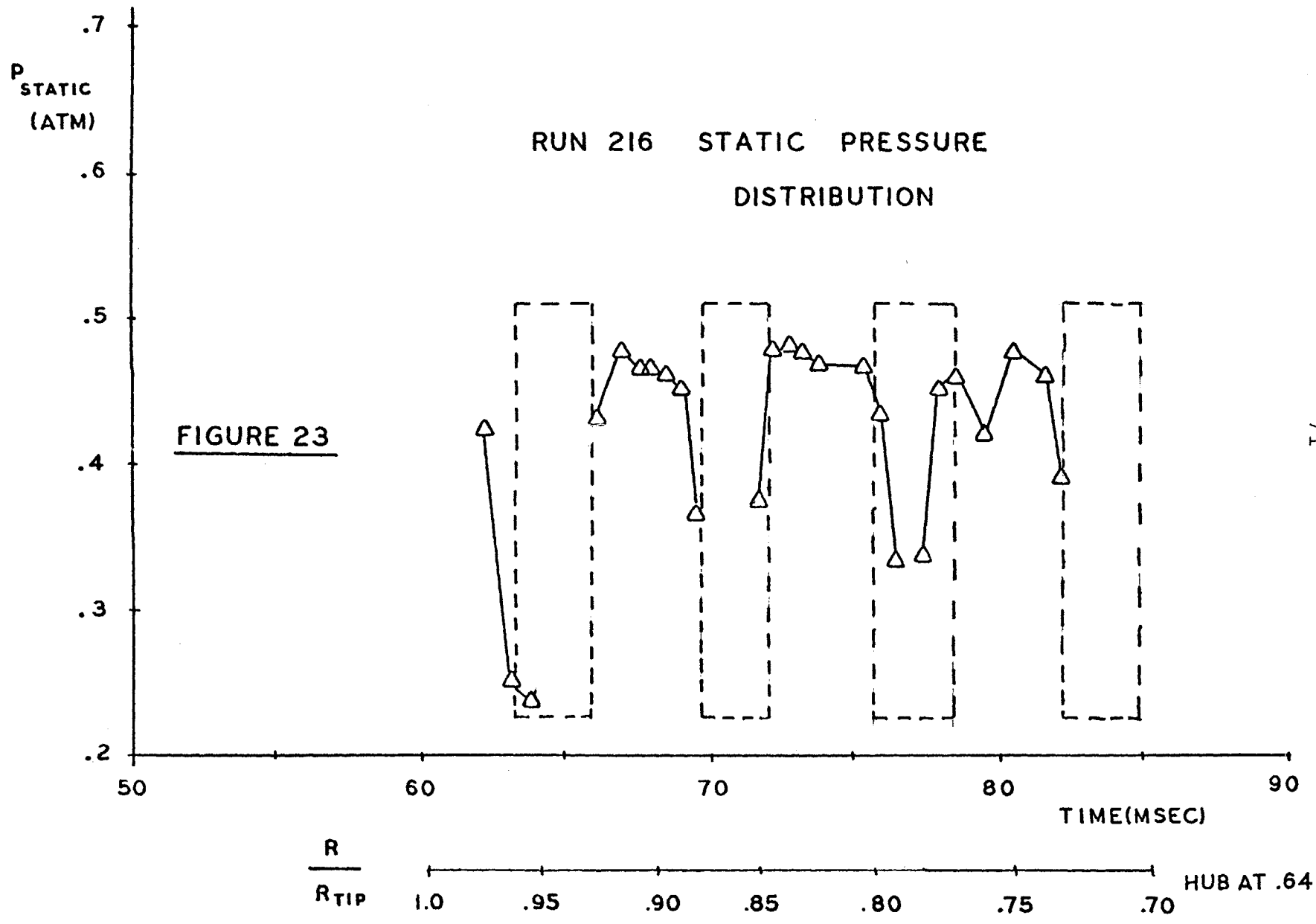
RUN 216

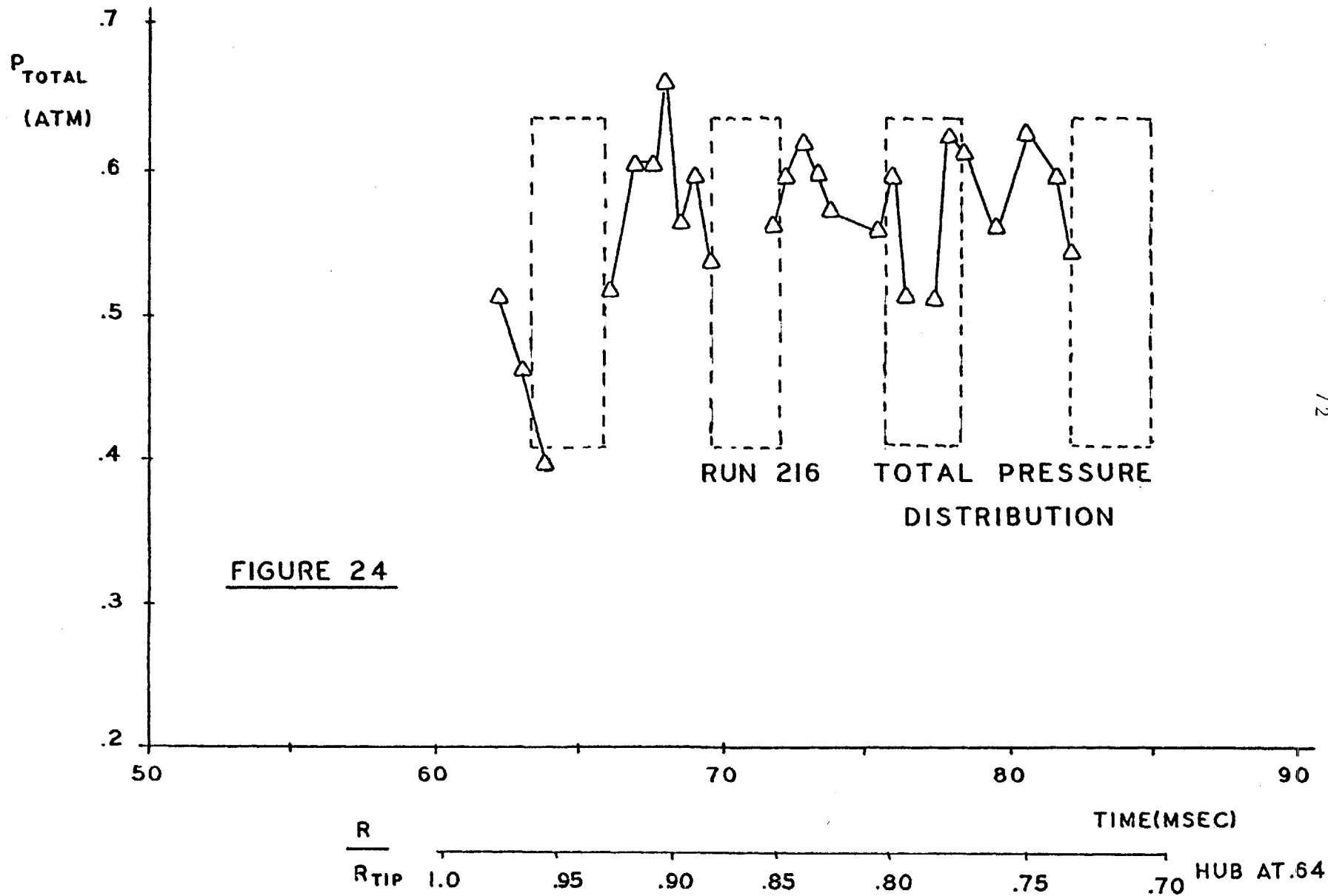


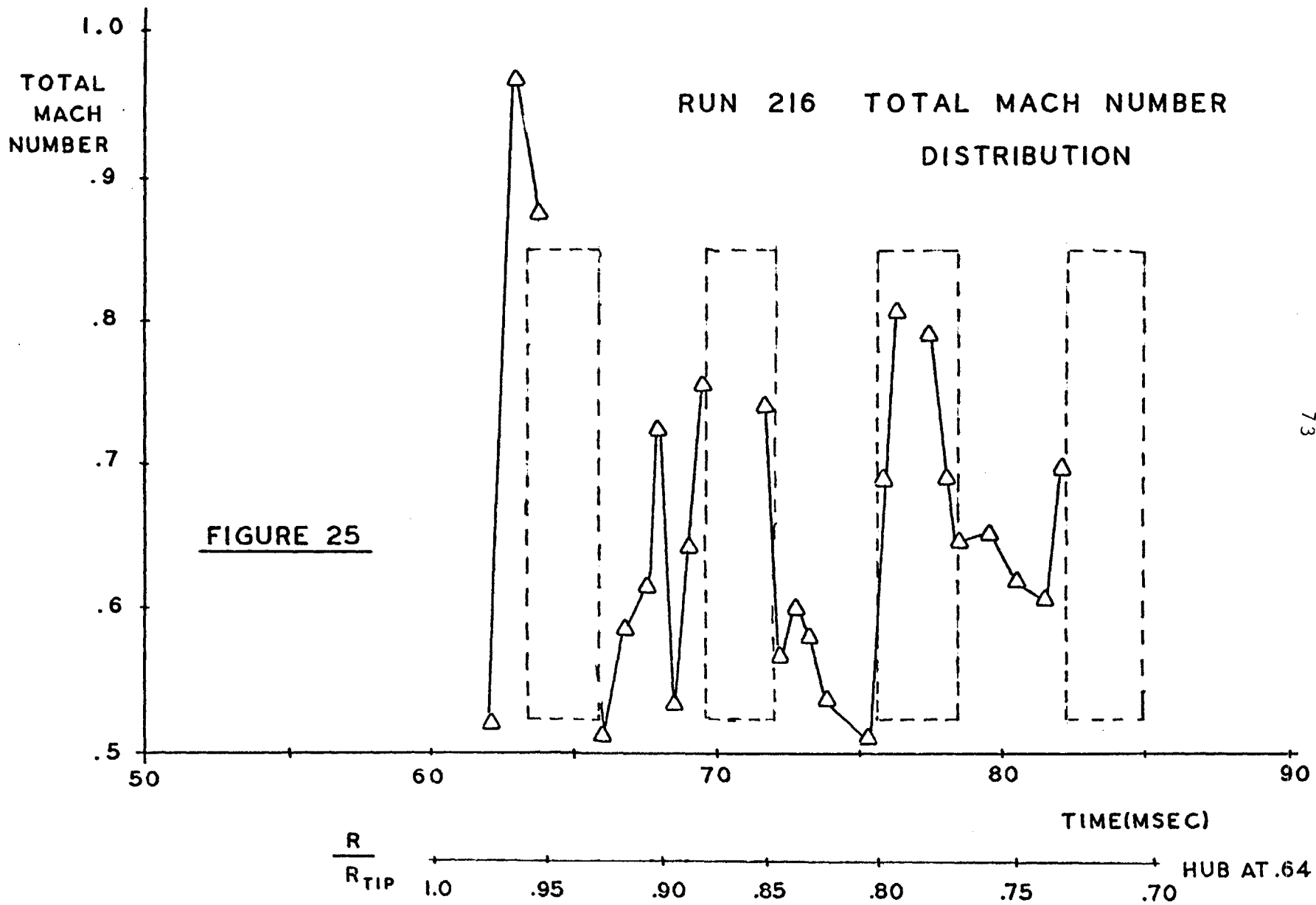


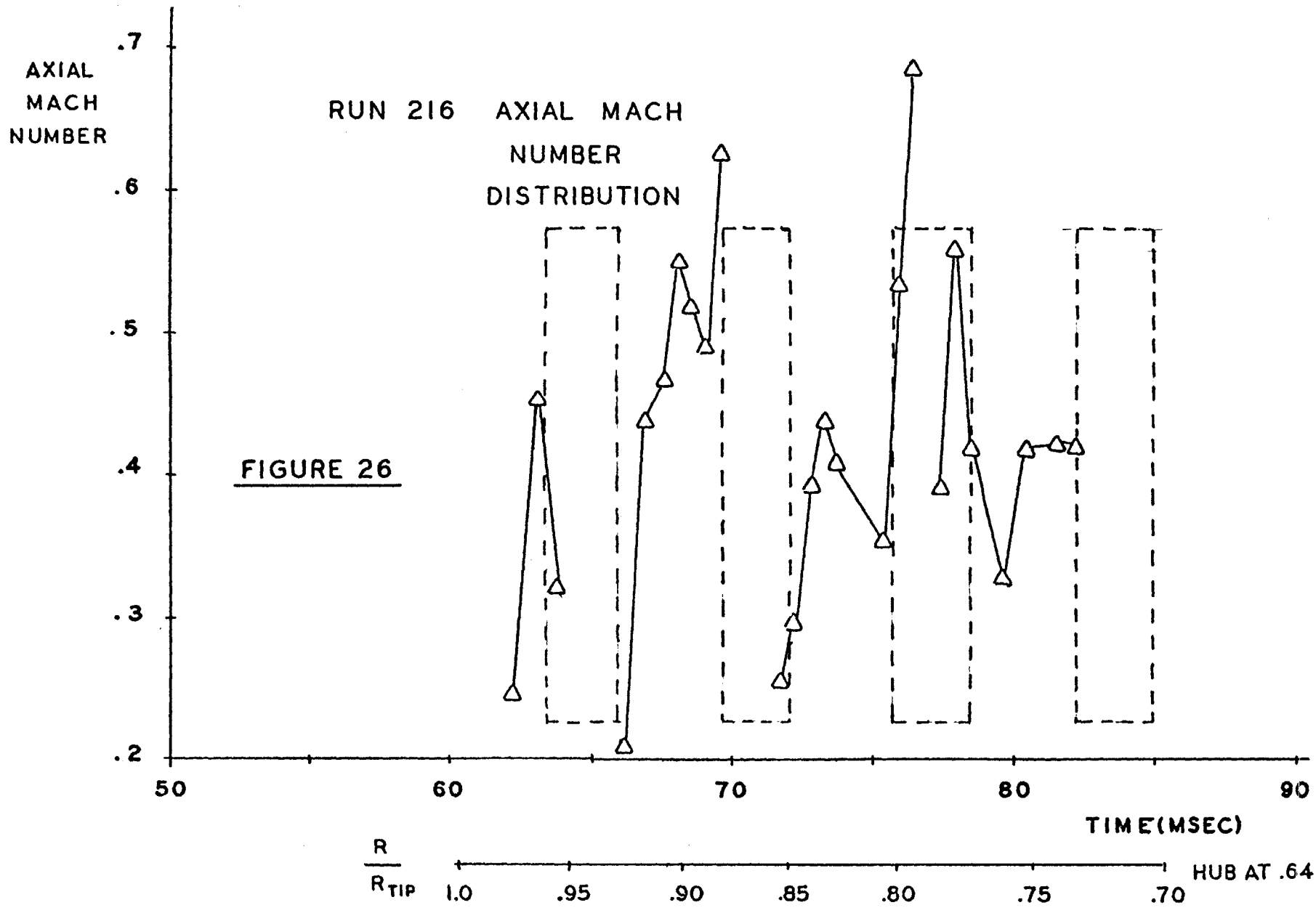


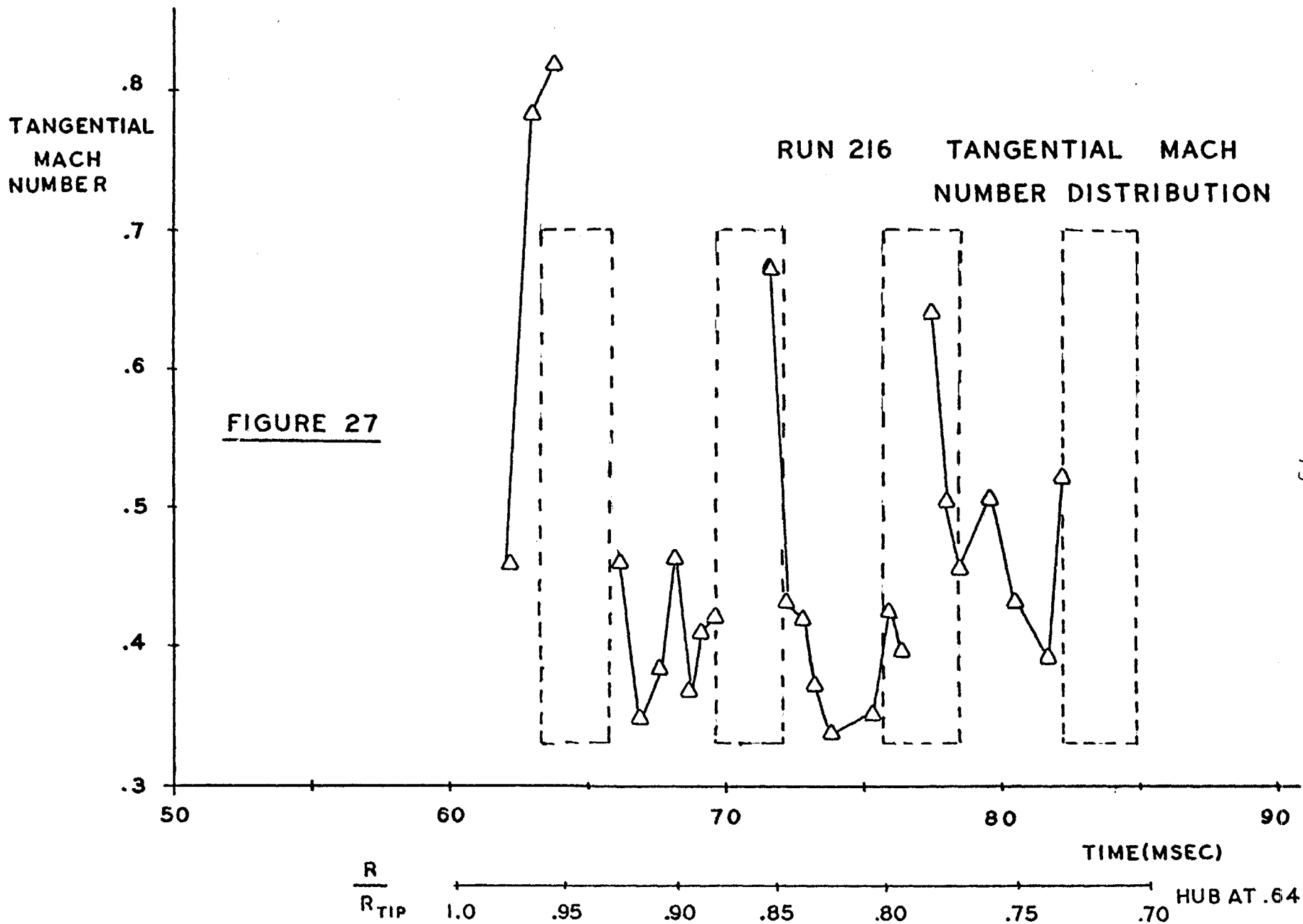












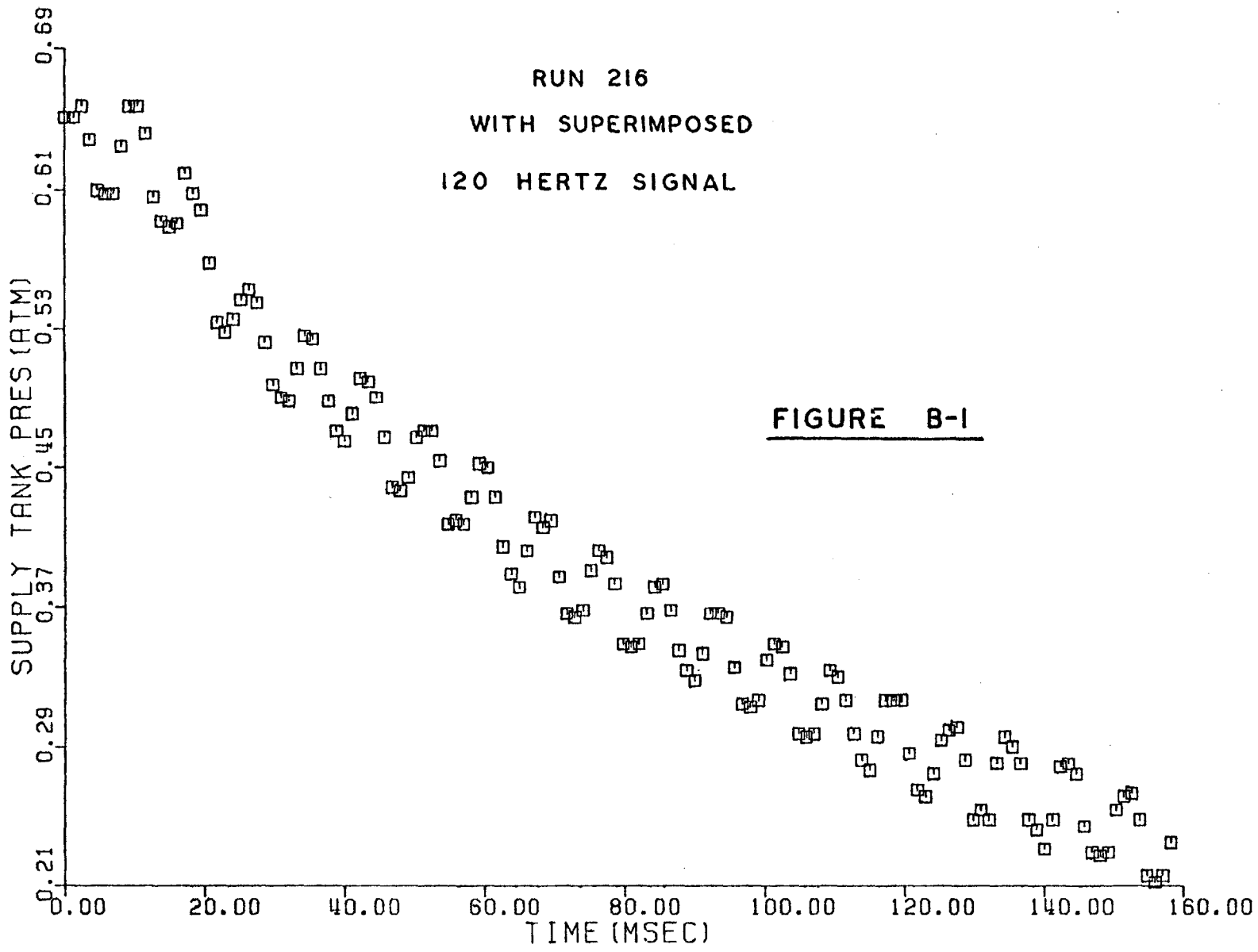


FIGURE B-2

RUN 216 SUPPLY TANK PRESSURE

FREQUENCY-AMPLITUDE

SPECTRUM

